JGR Atmospheres

RESEARCH ARTICLE
10.1029/2022JD038133

The Diurnal Cycle of East Pacific Convection, Moisture, and CYGNSS Wind Speed and Fluxes

Emily M. Riley Dellaripa[1], Eric D. Maloney[1], and Charlotte A. DeMott[1]

[1]Department of Atmospheric Science, Colorado State University, Fort Collins, CO, USA

Key Points:

- An index is developed to distinguish between days with strong versus weak westward-propagating diurnal precipitation in the far east Pacific
- Strongly propagating days have increased low-level moisture, regional circulations, and gap winds relative to weakly propagating days
- Cyclone Global Navigation Satellite System measurements show that increased moisture on the strongly propagating days is supported by increased wind-induced latent heat fluxes

Correspondence to:
E. M. Riley Dellaripa,
Emily.Riley@colostate.edu

Citation:
Riley Dellaripa, E. M., Maloney, E. D., & DeMott, C. A. (2023). The diurnal cycle of east Pacific convection, moisture, and CYGNSS wind speed and fluxes. *Journal of Geophysical Research: Atmospheres*, *128*, e2022JD038133. https://doi.org/10.1029/2022JD038133

Received 7 NOV 2022
Accepted 28 MAR 2023

Author Contributions:
Conceptualization: Emily M. Riley Dellaripa, Eric D. Maloney
Formal analysis: Emily M. Riley Dellaripa
Funding acquisition: Eric D. Maloney
Methodology: Emily M. Riley Dellaripa, Eric D. Maloney, Charlotte A. DeMott
Supervision: Eric D. Maloney, Charlotte A. DeMott
Visualization: Emily M. Riley Dellaripa
Writing – original draft: Emily M. Riley Dellaripa
Writing – review & editing: Eric D. Maloney, Charlotte A. DeMott

© 2023. The Authors.
This is an open access article under the terms of the Creative Commons Attribution License, which permits use, distribution and reproduction in any medium, provided the original work is properly cited.

Abstract The far eastern tropical Pacific is one of the rainiest locations on Earth. This region is characterized by a robust diurnal cycle with precipitation initiating over the Andes mountains in Colombia in the late afternoon and moving offshore overnight while organizing into mesoscale convective systems (MCSs). As the MCSs move westward, they can seed tropical easterly waves that develop into tropical cyclones. Novel measurements of near-surface wind speeds and latent heat flux (LHFLX) from the Cyclone Global Navigation Satellite System (CYGNSS) mission and ERA5 reanalysis are used to evaluate changes to regional flow patterns, moisture, and LHFLX that favor a strong westward propagating diurnal cycle of precipitation in this region. Days with strongly versus weakly westward propagating diurnal precipitation are compared during the extended boreal summer of the CYGNSS era (May–October 2018–2021). Strongly propagating days have a more moist lower troposphere with stronger vertically integrated moisture flux convergence than days with weakly propagating precipitation. The enhanced low-level moisture is supported by increased wind-driven LHFLX from stronger regional flows including the Choco and Caribbean Low-Level Jets and Panama and Papagayo gap winds. Increased offshore convergence and vorticity also help sustain convection during the days with strongly propagating precipitation. Background variations in the physical environment, as opposed to diurnal variations, seem more important for supporting a robust diurnal cycle of precipitation in the region.

Plain Language Summary The eastern tropical Pacific Ocean off the coast of Colombia is one of the rainiest locations on Earth. Thunderstorms frequently form in the late afternoon over the foothills of the Andes mountains and then move offshore into the eastern Pacific overnight and into the early morning while growing into bigger thunderstorms. These large thunderstorms are important because they can eventually lead to tropical cyclone development as they move westward over the eastern Pacific parallel to central America. We evaluate environmental conditions that favor days when thunderstorms move far away from the Colombian coast along central America versus days when thunderstorms stay closer to the Colombian coast. We find that days when the thunderstorms move farther away from the Colombian coast have more moisture near the Earth's surface. This enhanced moisture is supported by increased winds near the surface in the east Pacific and Caribbean that help transport moisture from areas near the Pacific equator and Caribbean to offshore of Colombia and transfer moisture from the far eastern Pacific Ocean surface into the overlying atmosphere. Measurements from eight microwave-size satellites in space were critical to determine the role of the transfer of moisture from the ocean surface to the atmosphere.

1. Introduction

The exceptional amount of rainfall that occurs in the far east Pacific off the western coast of Panama and Colombia has long been recognized (Murphy, 1939). Nichols and Murphy (1944) termed this region the Panama Bight due to the concave coastline. Rain gauges and satellite observations have confirmed this region as one of the rainiest spots in the world (e.g., Mapes, Warner, & Xu, 2003; Mapes, Warner, Xu, et al., 2003; Negri et al., 2000; Poveda & Mesa, 2000; Vallejo-Bernal et al., 2021). Recent data collected by the Global Precipitation Measurement (GPM) mission estimate rainfall amounts exceeding 1 mm hr^{-1} (Figure 1a) just off the coast of Colombia, while rain gauge measurements show even larger extreme rainfall between the Colombian coast and Andes mountains (Poveda & Mesa, 2000).

Heavy rainfall occurs year-round in the Panama Bight with maximum values from May to October (Hastenrath, 2002; Mapes, 2003a; Velasco & Fritsch, 1987) as peak insolation and the Intertropical Convergence Zone (ITCZ) migrate to the north of the equator. Accompanying the annual march of the ITCZ is the interaction of dynamics and thermodynamics with complex topography and sea surface temperature (SST) gradients that

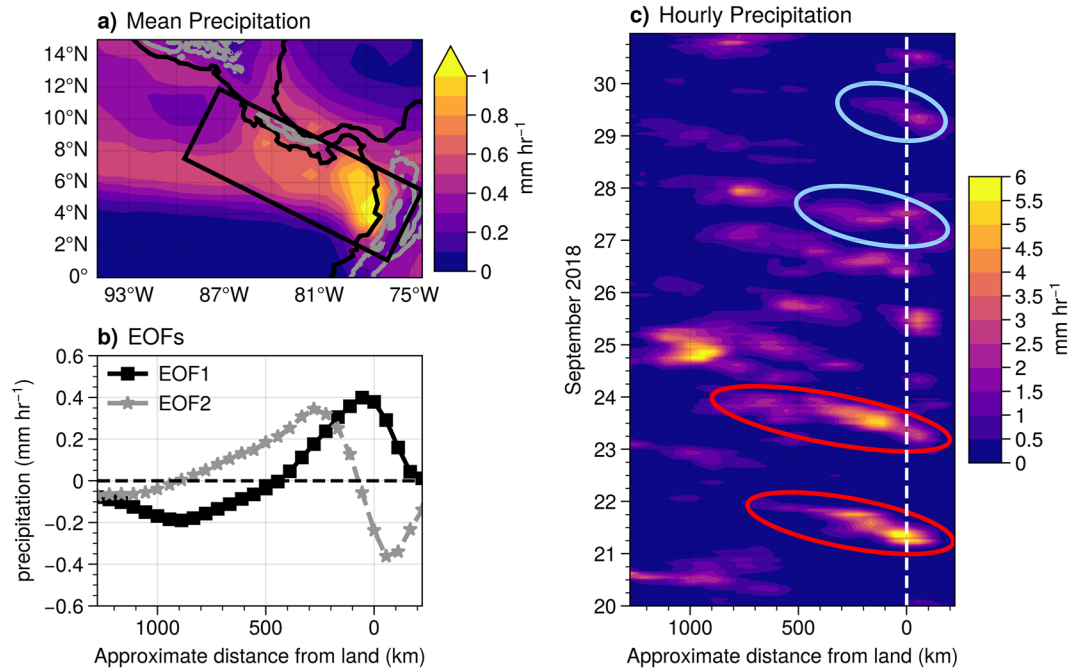

Figure 1. (a) Mean IMERG precipitation for May–October 2018–2021, excluding May–July 2018 and October 2021. Gray contour is 1-km topography. The rectangle represents the region used to determine strongly versus weakly propagating days. (b) EOF1 and EOF2 of rainfall averaged over the width of the rectangle in (a). (c) Distance versus time plot of IMERG precipitation from 20 to 30 September 2018. The *x*-axis in (b) and (c) represents the approximate distance from the Colombian coast along the long side of the rectangle shown in (a). In (c), red ellipses indicate examples of strongly propagating days, while blue ellipses indicate examples of weakly propagating days as defined by our index described in the text.

together produce abundant rainfall. In the far east Pacific, a strong SST gradient exists at the juncture of the equatorial cold tongue and the Panama Bight portion of the eastern Pacific warm pool. This SST gradient is associated with low-level cross-equatorial southwesterlies, known as the Choco Jet (Poveda & Mesa, 1999, 2000), which curves into the Colombian coast and brings abundant moisture to the Panama Bight and onshore (e.g., Amador et al., 2006; Poveda & Mesa, 2000). Additional moisture is delivered to the region via strong low-level easterly flow associated with the Caribbean Low-Level Jet (CLLJ; Amador, 1998; Amador et al., 2006; Cook & Vizy, 2010; Wang, 2007; Wang et al., 2007; Whyte et al., 2008) and gap winds through the Central American mountains. These gap winds include the Panama Jet off the Pacific coast of Panama (Figure 6c), the Papagayo Jet over the Gulf of Papagayo near the border of Nicaragua and Costa Rica (Figures 6a and 6c), and the Tehuantepec Jet over the Gulf of Tehuantepec near southern Mexico (e.g., Amador et al., 2006; Chelton et al., 2000; Serra et al., 2010). The moist air of the Choco Jet is met by the Andes mountains and undergoes orographic ascent and converges with the easterlies aloft from eastern South America (Poveda & Mesa, 2000; Poveda et al., 2014). The easterlies aloft are focused in a midtropospheric jet between 700 and 600 hPa that brings additional moisture to the far east Pacific from the Atlantic Ocean after crossing northern South America (Poveda et al., 2014).

Thermal contrasts in daytime heating between the land and ocean lead to stronger onshore flow during the day (i.e., sea breeze) and weaker offshore flow overnight (i.e., land breeze) and help give the region a robust diurnal cycle of precipitation. The enhanced daytime onshore flow and heating help destabilize the atmosphere over the coastal region and foothills leading to enhanced precipitation during the late afternoon (Garreaud & Wallace, 1997; Mapes, Warner, Xu, et al., 2003; Poveda & Mesa, 2000; Poveda et al., 2005; Zuluaga & Houze, 2015). Overnight and into the morning, precipitation moves offshore and propagates westward while growing upscale into mesoscale convective systems (MCSs; Jaramillo et al., 2017; Mejia & Poveda, 2005; Velasco & Fritsch, 1987; Zuluaga & Houze, 2015). The triggering of late afternoon convection over land by sea-breeze circulations and forced orographic ascent followed by offshore propagation through land breeze and/or gravity-wave dynamics and MCS development is well known throughout the tropics (e.g., Bai et al., 2021; Houze, 2012; Kirshbaum et al., 2018; Natoli & Maloney, 2019; Park et al., 2011; Qian, 2008; Riley Dellaripa et al., 2020; Wu et al., 2008; Yokoi et al., 2017; Zhou & Wang, 2006).

MCSs account for a majority of the precipitation in the Panama Bight and are largely responsible for the maximum in diurnal precipitation off the Colombian coast (Figure 1; Jaramillo et al., 2017). Some studies hypothesize that the growth of offshore MCSs in the Panama Bight is due to gravity-wave dynamics (Mapes, Warner, & Xu, 2003; Yepes et al., 2020). Daytime heating initiates gravity waves that radiate from the elevated terrain of the Andes mountains. By early morning, the cool phase of the gravity wave reduces convective inhibition offshore and encourages MCS development (Mapes, Warner, & Xu, 2003; Yepes et al., 2020). Offshore-MCS development and propagation by a gravity-wave mechanism is ubiquitous across the tropics (e.g., Bai et al., 2021; Hassim et al., 2016; Vincent & Lane, 2016; Yokoi et al., 2017). Overnight land-breeze circulations along the Colombian coast may also aid offshore propagation of precipitation (e.g., Bai et al., 2021; Ho et al., 2008; Houze et al., 1981; Park et al., 2011; Zhou & Wang, 2006) by reducing the onshore flow from the Choco Jet and shifting moisture convergence offshore (Mejia et al., 2021).

Despite western Colombia and the Panama Bight having a prime environment for precipitation, not all days have strong diurnal cycles of precipitation that produce offshore westward-propagating MCSs (Figure 1b; Mapes, Warner, Xu, et al., 2003; Mejia et al., 2021). Understanding the physical mechanisms that lead to days with strong versus weak diurnal precipitation and offshore propagation of MCSs into the Panama Bight is important as MCSs can develop into convectively coupled easterly waves (EWs) which can then seed tropical cyclones (TCs; Kerns et al., 2008; Rydbeck & Maloney, 2015; Rydbeck et al., 2017; Serra et al., 2010; Whitaker & Maloney, 2020). Diurnal convection in particular may be important for the transition of MCSs to EWs, as model sensitivity experiments showed that EW variance in the east Pacific was greatly reduced when diurnal convection was suppressed (Rydbeck et al., 2017). Further, the strength of the Choco Jet and Papagayo Jet may also be important for the transition of MCS convection into an EW (Whitaker & Maloney, 2020). One example of the transition of MCS activity in the far east Pacific into a TC during the Cyclone Global Navigation Satellite System (CYGNSS) era is Hurricane Felicia (14–20 July 2021). Felicia originated from an area of disturbed weather over the far east Pacific Ocean, Costa Rica, and Panama on 9 July 2021. The disturbance became better organized as it moved westward before developing into a tropical depression by 14 July 2021 (https://www.nhc.noaa.gov/data/tcr/).

A limited number of previous studies have examined the regional-scale conditions favoring strong westward propagation of diurnal disturbances in the Panama Bight. Sounding observations from Nuqui, Colombia during the Organization of Tropical East Pacific Convection (OTREC) field campaign (5 August to 25 September 2019; Fuchs-Stone et al., 2020) combined with ECMWF atmospheric reanalysis version 5 (ERA5; Hersbach, Bell, et al., 2020) showed that days with stronger diurnal MCS activity in the Panama Bight and coastal Colombia are associated with an enhanced CLLJ and Choco Jet and an anomalously strong low-level cyclonic circulation over Panama extending from the surface to ∼800 hPa (Mejia et al., 2021), consistent with previous results by Zuluaga and Houze (2015). The stronger regional circulations during active MCS days supported enhanced moisture along the western slopes of the Andes mountains during the evenings that was related to increased moisture flux convergence (MFC). During the morning hours of the active MCS days, the enhanced MFC shifted offshore promoting MCS growth and offshore propagation. Mejia et al. (2021) suggested that the increase in offshore MFC was due to the deceleration of the Choco Jet via overnight-to-morning land-breeze circulations. Increased low-to-midlevel wind shear and the generation of midlevel mesoscale convective vortexes (MCVs) were also hypothesized to be important for sustaining long lasting offshore-MCS development and propagation. WRF simulations of the Choco Jet Experiment (Yepes et al., 2019) time period also indicated enhanced low-to-midlevel wind shear may help delineate days with versus without offshore westward propagating precipitation. Similar wind and moisture variations were found by Zuluaga and Houze (2015).

Though the previous studies give a thorough analysis of the local and regional environmental mechanisms responsible for diurnal precipitation in the Panama Bight and coastal Colombia, not all environmental drivers have been explored, and some of the results were derived over a limited time period. Notably missing is the role of air-sea feedbacks in supporting diurnal westward propagating precipitation in the region. The atmosphere and ocean are energetically coupled by latent and sensible heat fluxes, with latent heat fluxes (LHFLXs) considerably larger than sensible heat fluxes in the region and in the tropics in general (e.g., Amador et al., 2006; DeMott et al., 2015; Riley Dellaripa & Maloney, 2015). Prior work has found that LHFLXs are enhanced with gust fronts generated by oceanic tropical convection (e.g., Redelsperger et al., 2000; Riley Dellaripa & Maloney, 2018; Wu & Guimond, 2006; Young et al., 1995). However, the importance of enhanced wind-induced LHFLXs for supporting mesoscale convection is less clear. For example, Tobin et al. (2012) and Tompkins and Craig (1998) found that increased surface fluxes aid mesoscale convective organization, while Gentine et al. (2016) and

Riley Dellaripa et al. (2018) came to an opposite conclusion. Idealized simulations suggest that flux feedbacks may be important in the initial stages of convective organization, but not for maintaining organization (Holloway & Woolnough, 2016; Wing & Cronin, 2016; Wing & Emanuel, 2014).

The previous studies discussing wind-induced LHFLX feedbacks on convective development relied on spatially or temporally sparse observations (i.e., Araligidad & Maloney, 2008; Bui et al., 2020; Riley Dellaripa & Maloney, 2015; Tobin et al., 2012) or idealized model simulations (i.e., Gentine et al., 2016; Holloway & Woolnough, 2016; Tompkins & Craig, 1998; Wing & Cronin, 2016; Wing & Emanuel, 2014). The launch of CYGNSS in December 2016 offers a new opportunity to observe oceanic surface wind speeds (Ruf et al., 2016) and derive tropical LHFLXs (Crespo et al., 2019) on a high temporal (i.e., approximate 3-hr revisit time) and spatial (i.e., 25-km effective resolution) scale (Ruf et al., 2019; Stephens et al., 2020). Consisting of a constellation of eight low-Earth orbit (i.e., 510-km altitude and 35° inclination) microsatellites, CYGNSS measures wind speeds over the ocean by detecting direct and reflected Global Positioning System (GPS) signals from the ocean surface. Each satellite can detect signals from at most four GPS satellite transmitters thus giving the constellation 32 simultaneous wind-speed measurements. CYGNSS can detect wind speed in any weather condition as GPS L-band microwave-channel (19-cm wavelength; 1,575 MHz) signals are not appreciably affected by rainfall (Balasubramaniam & Ruf, 2020). This is a distinct advantage over traditional spaceborne scatterometer-based wind retrievals that rely on measuring the backscatter power from a radar pulse (e.g., Weissman et al., 2012; Wentz et al., 1982).

Taking advantage of CYGNSS unique observing capabilities, this study aims to evaluate the role of wind-induced LHFLXs for supporting westward-propagating diurnal convective systems off the Colombian coast and their link to moisture variations in the Panama Bight. We examine the relative importance of diurnal versus background variations in wind, moisture, and LHFLXs for supporting the westward propagation of precipitation in the Panama Bight by comparing composites of those environmental variables during days in the CYGNSS era that have strong westward propagation of precipitation from the Colombian coast into the Panama Bight, versus those that do not.

The following section describes the CYGNSS data and ERA5 reanalysis used for this study, as well as our method for isolating strongly and weakly propagating days. Section 3 compares precipitation during the strongly versus weakly propagating days, while Section 4 discusses the moisture, wind, and LHFLX variations during those respective days. Sections 5 and 6 discuss and summarize the paper, respectively.

2. Data and Methodology

2.1. CYGNSS Data

The CYGNSS science team offers two wind speed products—a science data record (SDR) and a climate data record (CDR). The CDR wind speeds have a trackwise correction that removes biases due to variations in GPS transmit power and other factors (Ruf & Twig, 2020; Said et al., 2019). The correction relies on reanalysis products and is therefore not a completely independent wind-speed sample (Pascual, Clarizia, & Ruf, 2021; Ruf & Twig, 2020). Additionally, the correction cannot be applied to all CYGNSS data resulting in fewer wind-speed samples. We, therefore, use the latest level-2 SDR wind speed product, SDR version 3.1 (SDR 3.1; CYGNSS, 2021), which includes spatially averaged wind speed at a 25 × 25-km grid spacing (Pascual, Clarizia, Zavorotny, et al., 2021).

Data are available from 1 August 2018 to the present. Though science data collection started in March 2017, prior to 1 August 2018, the CYGNSS receivers did not include real-time monitoring and correction of variations in GPS transmit power, which were necessary to maximize retrievals from GPS satellites (Ruf & Balasubramaniam, 2019; Ruf & Twig, 2020; Wang et al., 2022). We use the fully developed seas (FDS) estimates of wind speed, which assumes the sea surface is at equilibrium with the wind speed. CYGNSS wind speeds agree well with tropical buoy observations (Asharaf et al., 2022).

We also used the CYGNSS level-2 SDR surface LHFLX product version 2.0 (CYGNSS, 2022) that derives fluxes using version 3.5 of the Coupled Ocean-Atmosphere Experiment (COARE) bulk flux algorithm (Edson et al., 2013; Fairall et al., 2003) with inputs from level-2 SDR 3.1 wind speeds and ERA5 specific humidity and near-surface air and SST (Crespo et al., 2019). The CYGNSS LHFLXs are provided with a 25 × 25-km grid spacing for the same times and locations as the wind-speed measurements. CYGNSS LHFLXs agree well with

LHFLXs from tropical buoys with a correlation near 0.8 (Crespo et al., 2019). Both the CYGNSS wind speed and LHFLX were regridded to an hourly 1° × 1° grid using the technique outlined in Ruf (2018).

2.2. ERA5 Reanalysis Data

The CYGNSS near-surface wind speeds were complemented with ERA5 winds. The 1,000-hPa and 925-hPa winds detail variations in the Choco Jet, which is traditionally defined at 925 hPa (e.g., Poveda & Mesa, 2000; Poveda et al., 2014; Yepes et al., 2019) since zonal winds just off the Colombian coast maximize at that level. The 1,000-hPa winds are compared to the CYGNSS wind speeds, which are only available at the surface. The 850-hPa winds are used to detect changes in the CLLJ and gap winds between the strongly and weakly propagating days. Lastly, the 650-hPa winds reveal how the easterly midtropospheric jet above the Andes mountains (e.g., Poveda et al., 2014) varies with changes in the diurnal cycle of precipitation.

Vertical profiles of ERA5 winds and specific humidity were used to evaluate variations of low-level divergence and vorticity, vertical profiles of moisture, and vertically integrated moisture flux convergence (VIMFC) as prior work (i.e., Mejia et al., 2021; Zuluaga & Houze, 2015) has suggested that enhanced surface convergence and low-to-midlevel vorticity and moisture help support MCS development and its westward propagation in the Panama Bight. Hourly and global ERA5 variables with a native 0.25° × 0.25° grid spacing (Hersbach, Bell, et al., 2020; Hersbach et al., 2018a, 2018b), were regridded to 1° × 1° to match the gridded CYGNSS data.

2.3. Method for Isolating Strongly Versus Weakly Propagating Days

Precipitation estimates from NASA's Integrated Multi-satellitE Retrievals for Global Precipitation Measurement (GPM IMERG) final-version 6 product (Huffman, Bolvin, et al., 2019; Huffman, Stocker, et al., 2019) are used to determine days in the Panama Bight that have strong versus weak diurnal precipitation. IMERG precipitation (Huffman, Bolvin, et al., 2019) was regridded from its native 30 min, 0.1° × 0.1° grid to an hourly, 1° × 1° grid to match the gridded CYGNSS wind speeds. We analyzed days from May to October of the CYGNSS era (i.e., August 2018 to present), which specifically includes August–October 2018, May–October 2019 and 2020, and May–September 2021. October 2021 is not included because the IMERG final-version 6 product ends in September of 2021, and no plans exist to process more months until the final-version 7 is available (Huffman, Stocker, et al., 2019). We restrict our analysis to May to October as those are the months when rainfall is greatest in the Panama Bight (Amador et al., 2006; Mapes, Warner, Xu, et al., 2003) and also overlaps with the local TC season (Amador et al., 2006).

Figure 1a shows the average precipitation for available days during May–October 2018–2021. Consistent with previous studies (Mapes, Warner, Xu, et al., 2003), maximum precipitation occurs offshore of Colombia and extends northwest along the coast of Central America. The average ITCZ position further west is centered about 7°N. Precipitation enclosed within the black rectangle (Figure 1a) was used to determine days when diurnal precipitation had strong versus weak westward propagation from Colombia into the Panama Bight. Precipitation was first averaged over the width (i.e., shorter dimension) of the rectangle. Then, the hourly precipitation for each day was normalized by each day's mean precipitation over the entire rectangle. Finally, the time series of the normalized, width-averaged precipitation was decomposed into empirical orthogonal functions (EOFs). The two leading EOFs depict precipitation centered just inland of the Colombian coast and ∼250 km offshore (Figure 1b). Together, these first two EOFs explain 44.8% of the variance. The principal components (PCs) associated with the leading EOFs have a maximum correlation of 0.3 at a lag of 6 hr. We define days as having strongly propagating diurnal precipitation when a maximum in PC1 occurs between 00 and 12 UTC, which is 19-07 local time (LT) that exceeds one standard deviation (1σ) followed by a maximum in PC2 that exceeds 1σ within 12 hr of the PC1 maximum. If there is no maximum in PC2 within 12 hr of the PC1 maximum, then the day is classified as having weakly propagating diurnal precipitation. We refer to these days as strongly and weakly propagating days. A similar method was used by DeMott et al. (2018) to define Madden-Julian Oscillation (MJO) events that propagated through versus decayed at the Maritime Continent (MC). The results are robust to varying the cutoff time for the PC1 maximum and altering the lag period between the PC1 and PC2 maximum. Performing the EOF decomposition on absolute precipitation values did not adequately distinguish between days with strong versus weak diurnal precipitation. Our method assumes that the westward propagation follows the path of mean precipitation, i.e., along the length (or long side) of the box in Figure 1a and could miss offshore propagation that was not aligned with the box.

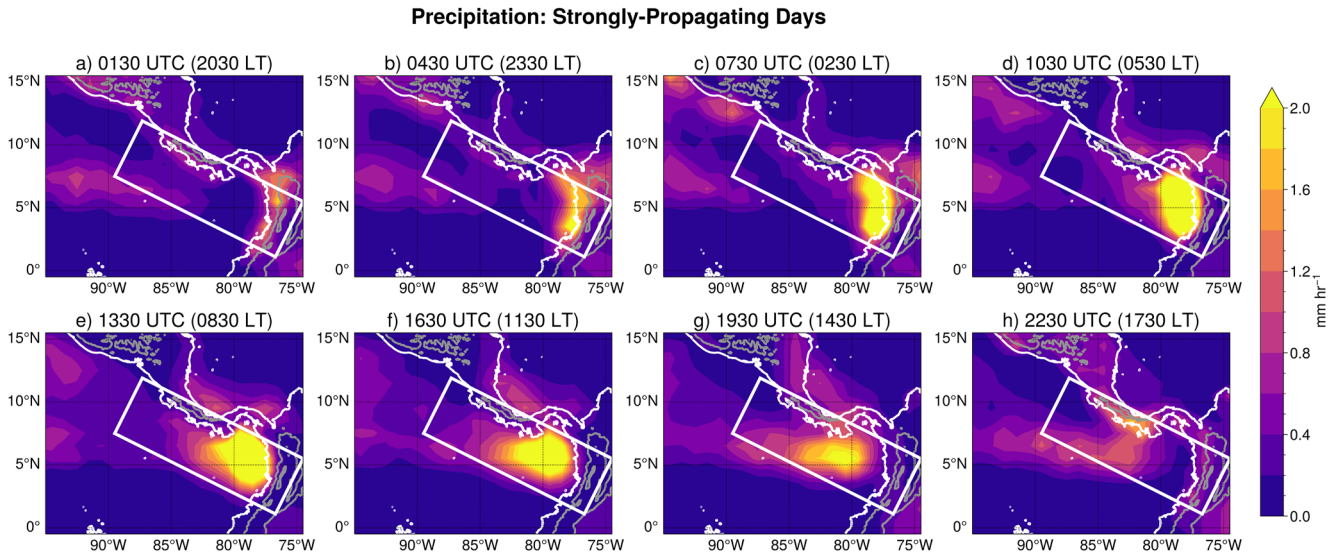

Figure 2. Three-hourly composite of IMERG precipitation for strongly propagating days. Gray contour represents 1-km topography. The white rectangle indicates the region used to construct distance versus time plots in the following figure.

Figure 1c provides an example of days that qualify as strongly versus weakly propagating during 20–30 September 2018. We note that not all days qualify as either having strongly or weakly propagating precipitation. Of the 613 days included in the study, 159 were classified as strongly propagating, while 108 were classified as weakly propagating. We also analyzed days that had precipitation that originated offshore (i.e., PC1 $< 1\sigma$ and PC2 $> 1\sigma$) to ensure that the environmental conditions that favor precipitation that strongly propagates offshore are in fact important for encouraging strong offshore propagation and not simply favorable for any offshore precipitation. There were 126 days with offshore precipitation and we discuss our findings in the context of those days. We explored comparing wet versus dry days based on days that had 1σ above or below the mean precipitation inside the lower half of the rectangle. However, while the dry days showed very little diurnal precipitation over Colombia, there was still appreciable rainfall offshore that did not propagate and our focus here is on propagating precipitation originating over Colombia.

3. Precipitation During Strongly and Weakly Propagating Days

Figure 2 shows 3-hourly composites of precipitation for strongly propagating days. As shown in previous studies, inland precipitation forms along the foothills of the Andes mountains in the late afternoon and evening (Figures 2g and 2h). The convective region grows in intensity and size as it moves offshore overnight and into the early morning hours (Figures 2a–2e). From midmorning into the afternoon, the offshore precipitation weakens as it moves away from Colombia. Precipitation during the weakly propagating days has a similar evolution, except that the precipitation wanes closer to the Colombian coast. The differences in the extent of northwestward propagation of diurnal precipitation for strongly versus weakly propagating days are seen in time versus distance-from-shore plots (Figure 3) constructed by averaging over the width of the rectangle in Figure 2. The diurnal evolution of precipitation for all days considered in this study is also shown for comparison. During both subsets of days, precipitation maximizes in the early morning hours (10:30 UTC; 05:30 LT) just off the Colombian coast. However, the strongly propagating days have appreciable precipitation magnitudes (e.g., the 1 mm day^{-1} contour) that extend more than twice as far offshore as during the weakly propagating days (Figures 3b and 3c).

4. Moisture, Winds, and LHFLX Variations

Figure 4 shows 3-hourly composites of the differences in 1,000-600 hPa vertically integrated ERA5 specific humidity and IMERG precipitation between the strongly and weakly propagating days. For clarity, only the positive precipitation differences are shown. The decision to integrate over 1,000-600 hPa is based on vertical cross-sections of specific humidity differences inside the rectangle (Figure 2) that show moisture differences

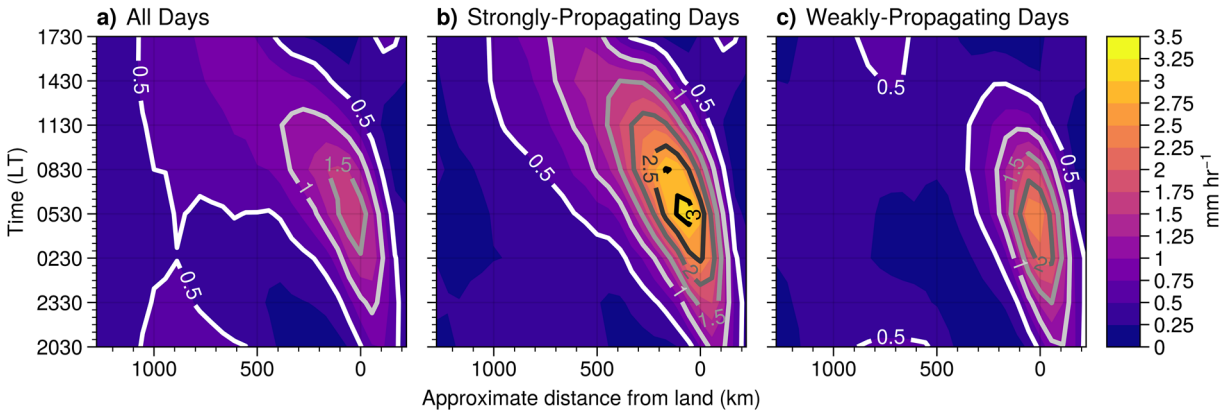

Figure 3. Distance versus time plots of diurnal-cycle composites of IMERG precipitation (shading and contours) averaged over the width (i.e., short side) of the rectangles shown in Figures 1 and 2 for (a) all days, (b) strongly propagating days, and (c) weakly propagating days. The *x*-axis represents the approximate distance from the Colombian coast along the length (i.e., long side) of the rectangle shown in Figures 1 and 2.

between strongly and weakly propagating days are largest at those levels (Figure 5). During the strongly propagating days, enhanced precipitation in the Panama Bight is accompanied by increased low-level moisture throughout the east Pacific southward of 8°N (Figure 4). The largest positive moisture differences are generally to the west and southwest of the maximum precipitation differences. Vertical cross-sections of moisture differences further detail that the offshore moisture enhancements during the strongly propagating days are relatively persistent and stationary throughout the day with the largest differences above the boundary layer (~850 hPa) ~300 km offshore (Figure 5). These findings are consistent with observations from Nuqui, Colombia during "wet" days of the OTREC field campaign that showed enhanced moisture below 4 km for the 00 UTC soundings (Majia et al., 2021).

The red and blue circles in each panel in Figure 5 indicate the location of maximum precipitation for strongly and weakly propagating days, respectively, according to the time-distance plots shown in Figures 3b and 3c. Note, the location of maximum precipitation for the weakly propagating days only considered precipitation <500 km from shore to avoid identifying precipitation that originated offshore (e.g., 0.5 mm hr^{-1} contours near 750 km). During the daytime hours (Figures 5e–5h), precipitation moves several hundred more kilometers offshore during the strongly propagating days compared to the weakly propagating days. The difference in the extent of propagation

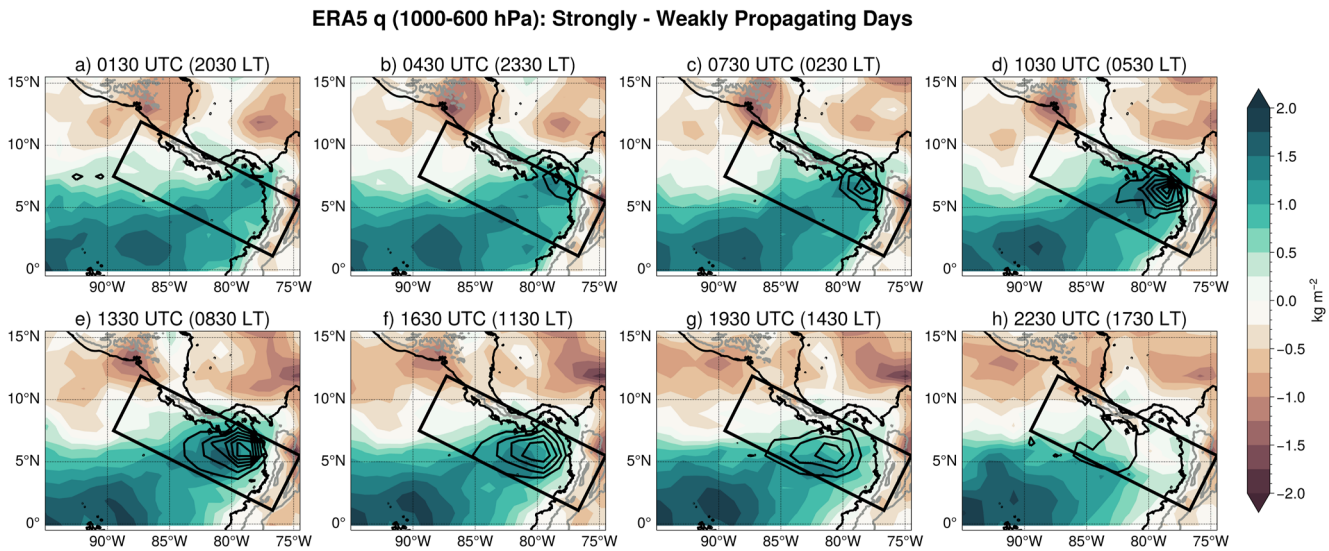

Figure 4. Three-hourly composites of mass-weighted vertically integrated (1,000-600 hPa) ERA5 specific humidity (shading) differences for strongly and weakly propagating days overlaid with IMERG precipitation differences in black contours starting at 0.5 mm hr^{-1} and incrementing by 0.5 mm hr^{-1}. Gray contours represent 1-km topography. The black rectangle indicates the region used to construct distance versus height plots in the following figure.

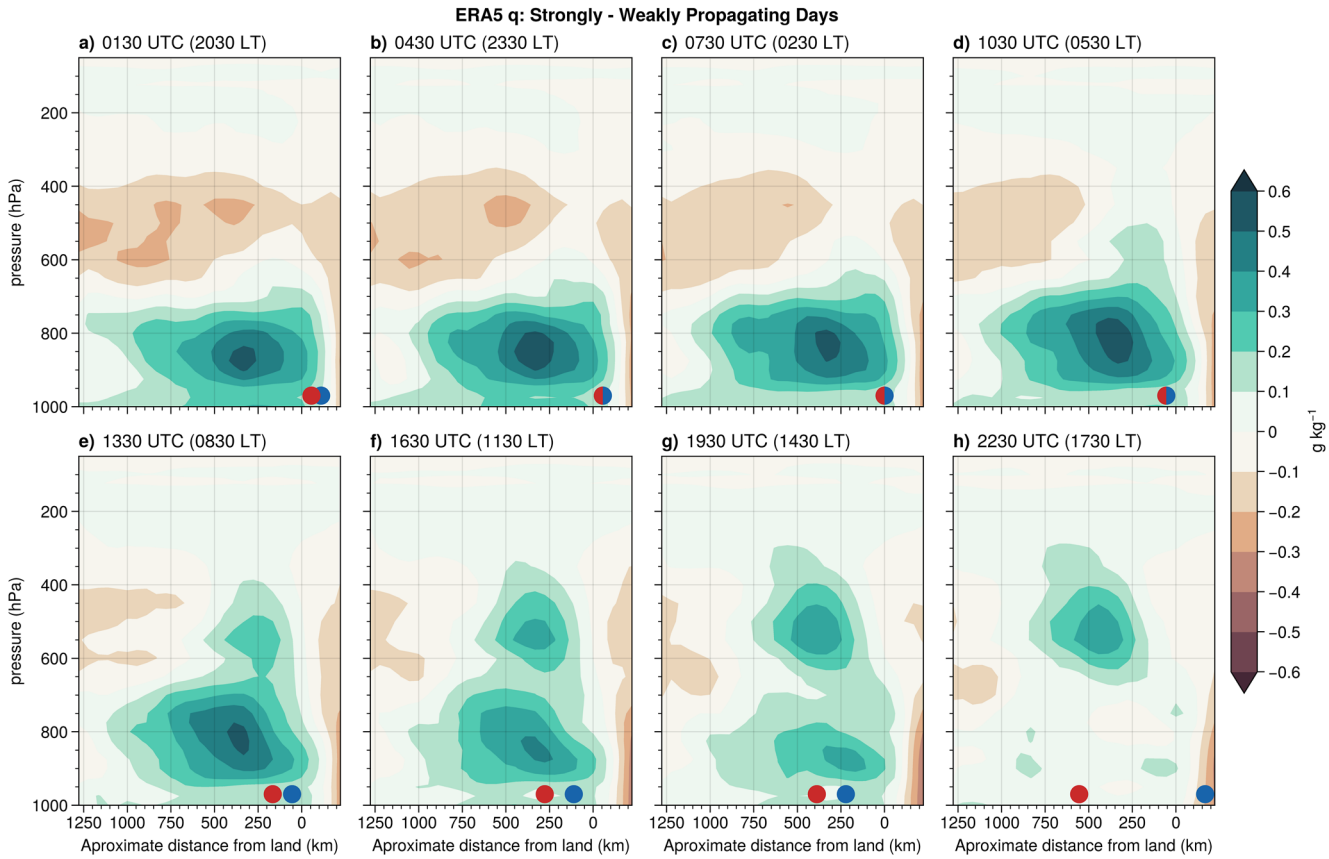

Figure 5. Three-hourly vertical cross-section of specific humidity differences for strongly and weakly propagating days averaged over the width (i.e., short side) of the rectangle shown in Figures 1 and 2. Circles are the location of maximum precipitation according to the Hovmollers shown in Figures 3b and 3c during strongly (red) and weakly (blue) propagating days. See text for details on how the maximum precipitation location was calculated. The *x*-axis represents the approximate distance from the Colombian coast along the long side of the rectangle shown in previous figures.

may in part be due to the enhanced low-level (<600 hPa) moisture offshore during the strongly propagating days as Tulich and Mapes (2010) showed that low-level (<4 km) moisture variations are especially important for supporting convection. Aloft (400–600 hPa), moisture variations tend to evolve in tandem with precipitation, suggesting that daytime midlevel moistening on strongly propagating days (Figures 5e–5h) is a byproduct of convective activity, such as detrainment of cloud condensate to the environment.

We next compare the regional-scale circulations in the Panama Bight during the strongly versus weakly propagating days. The left panels of Figure 6 show the mean ERA5 wind speed (shading) and vectors at 1,000, 925, 850, and 650 hPa over all days considered in this study. As stated in Section 2.2, both 1,000-hPa and 925-hPa winds are examined to evaluate the Choco Jet. At 1,000 and 925 hPa, cross-equatorial southwesterlies in the east Pacific become more zonal as they curve into the Colombian coast and form the Choco Jet. The Choco Jet at 925 hPa is slightly more zonal near the Colombian coast compared to the 1,000-hPa winds. Also noticeable at 1,000 and 925 hPa are the strong easterlies in the Caribbean that make up the CLLJ (Figure 6a). The CCLJ is most apparent at 850 hPa where the strong easterlies cross central America through gaps in the mountain ranges (Figures 6a, 6c, and 6e). While there are hints of the CLLJ crossing central America at 1,000 and 925 hPa through a gap in the Cordillera mountains near 11°N (i.e., the Papagayo Jet; Figures 6a and 6c), the Papagayo Jet is more evident at 850 hPa (Figure 6e). At 850 hPa, the Panama Jet is also visible across the Isthmus of Panama and into the far east Pacific (Figure 6e). Aloft at 650 hPa, zonal easterlies are ubiquitous across the region (Figure 6g). Poveda et al. (2014) highlighted this level as a midtropospheric jet that connects moisture from the Atlantic to the Pacific after crossing northern South America.

The low-level regional-scale flows including the Choco Jet, the CLLJ, and the Papagayo and Panama Jets are enhanced with greater onshore flow into Colombia during the strongly propagating days (Figures 6b, 6d, and 6f).

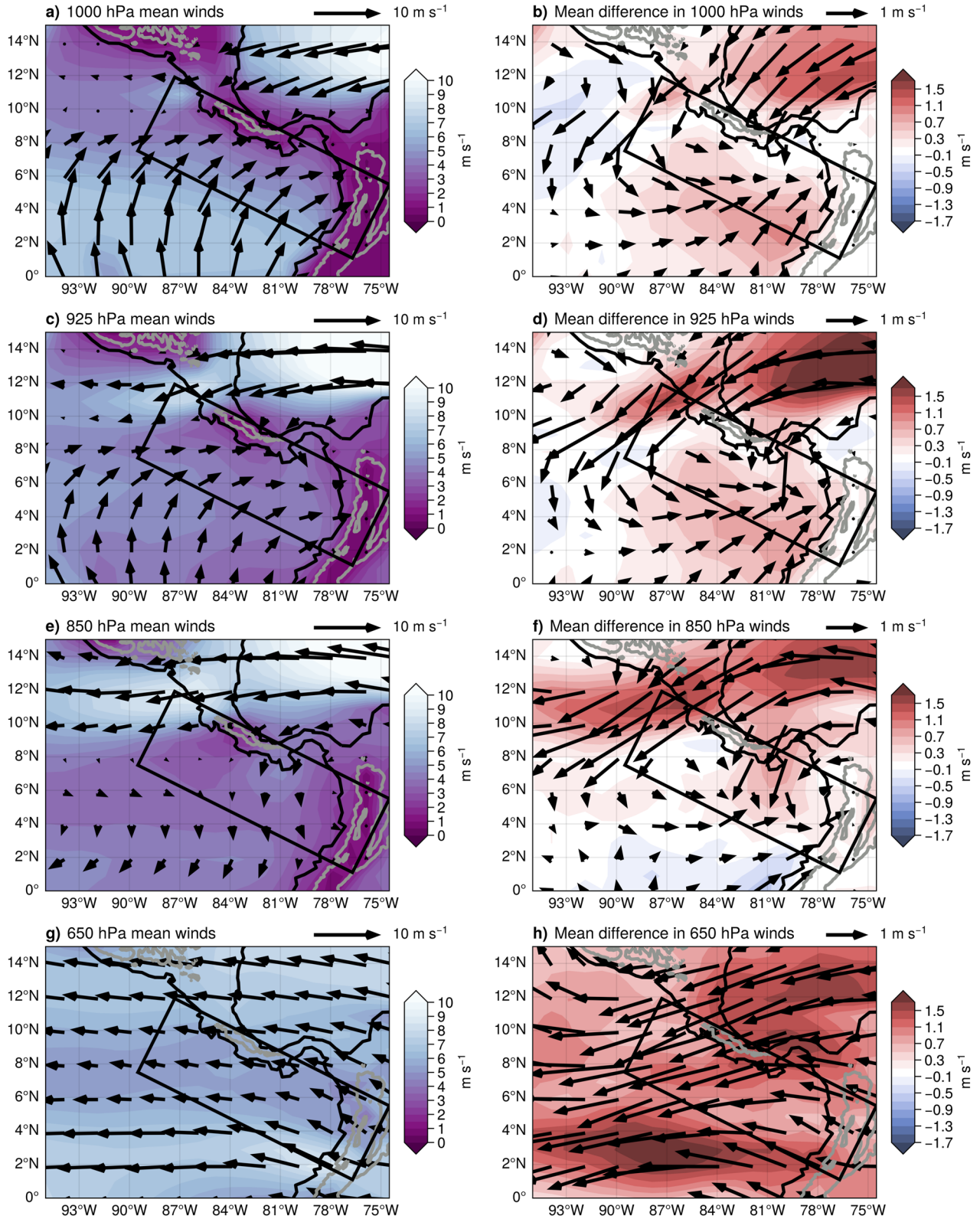

Figure 6. (a) The mean ERA5 1,000-hPa wind speed (shading) and vectors over all days in the data set (May–October 2018–2021). (b) The mean difference in 1,000-hPa wind speed (shading) and vectors between the strongly and weakly propagating days. (c) and (d) are the same as (a) and (b), except for at 850 hPa. Gray contours represent 1-km topography. The black rectangle indicates the region used to construct distance versus times plots in future figures.

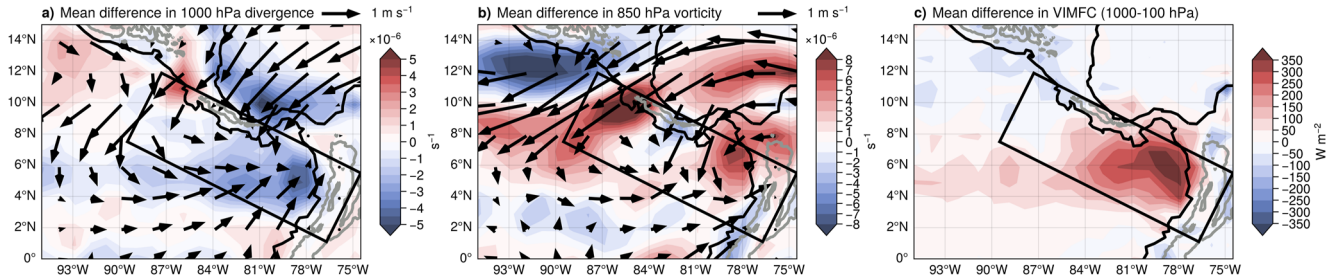

Figure 7. The shading represents the mean difference between strongly and weakly propagating days (a) 1,000-hPa divergence, (b) 850-hPa vorticity, and (c) vertically integrated moisture flux convergence from 1,000 to 100 hPa. The differences in wind vectors between the strongly and weakly propagating days at 1,000 and 850 hPa are overlaid in (a) and (b), respectively. Gray contours represent 1-km topography. The black rectangle indicates the region used to construct distance versus times plots in future figures.

The midtropospheric winds at 650 hPa are also stronger during the strongly propagating days especially off the Colombian coast along 3°N and over the Caribbean and Panama (Figure 6h). Enhanced regional flows during the strongly propagating days are accompanied by increased low-level convergence (Figure 7a) that supports increased low-level moisture and precipitation (Figure 4). Stronger 850 hPa vorticity (Figure 7b) in the Panama Bight during the strongly propagating days may also help sustain and/or generate new MCS activity offshore of Colombia (e.g., Whitaker & Maloney, 2020). However, the root of the enhanced vorticity could also lie within the increased diurnal precipitation such that a positive feedback exists that has the potential to lead to EW development (Rydbeck et al., 2017). Rydbeck et al. (2017) showed that MCSs in the Panama Bight can contribute to vorticity generation via stretching within growing EWs and that the suppression of diurnal precipitation impedes MCS growth and reduces EW variability in the region.

Differences in the VIMFC during the strongly versus weakly propagating days further relate variations in the regional circulation and moisture to precipitation differences (e.g., Seager et al., 2007; Trenberth & Guillemot, 1995). During the strongly propagating days, VIMFC is enhanced in a pattern that resembles the increase in low-level convergence and moisture (Figures 7c and 4). The stronger moisture flux into the Panama Bight likely contributes to the extended offshore propagation of precipitation during the strongly propagating days.

Similar to ERA5, CYGNSS wind speeds are greater in the Panama Bight and the Caribbean during the strongly propagating days (Figure 8). CYGNSS-based LHFLXs show a pattern of enhanced LHFLXs during the strongly propagating days that generally reflects the enhanced wind speeds (Figures 8 and 9), which is not surprising given that wind speed is the most dominant term in the LHFLX equation over tropical warm pool regions (DeMott et al., 2014, 2016; Hendon, 2005; Yokoi et al., 2014). Differences in diurnal fluctuations of wind speed and LHFLX in the Panama Bight are generally positive from 23:30 to 14:30 LT. An exception is at 05:30 LT, when precipitation differences are largest (Figure 8). As demonstrated by Riley Dellaripa et al. (2018), this behavior could be linked to enhanced cold pool activity driven by larger rain amounts on strongly propagating days. The westward expansion of cold pools initiated in the east Pacific could reduce surface fluxes mechanically by opposing background westerly winds, and thermodynamically by introducing more saturated air (via rain evaporation) into the boundary layer (e.g., Torri & Kuang, 2016). The exception at 05:30 LT could also be related to semidiurnal variability in atmospheric pressure and winds due to the semidiurnal cycle of the solar tide (e.g., Dai & Wang, 1999; Deser & Smith, 1998; Kohyama & Wallace, 2016; Ueyama & Deser, 2008). Ueyama and Deser (2008) found that the semidiurnal cycle in zonal winds peaks around 03:25 and 15:25 LT in the east Pacific, which roughly corresponds to the two times when wind speed and LHFLX differences are negative (Figures 8 and 9d, 9h). Its unclear, however, how or why the semidiurnal solar tide would lead to stronger winds (and thus LHFLX) during the weakly propagating days relative to the strongly propagating days during the tide's semidiurnal peaks.

Both the MFC and LHFLX help sustain moisture in the region against the drying effects of precipitation. Figures 4 and 5 indicate that there is stronger drying during the strongly propagating days as offshore low-level (>700 hPa) moisture differences weaken from midday into the evening (11:30–17:30 LT; Figures 4f–4h and 5f–5h) from their peak during the early morning hours (05:30 LT; Figures 4d and 5d). The enhanced drying on strongly propagating days could arise from greater loss of water vapor through precipitation formation, or from advection of drier

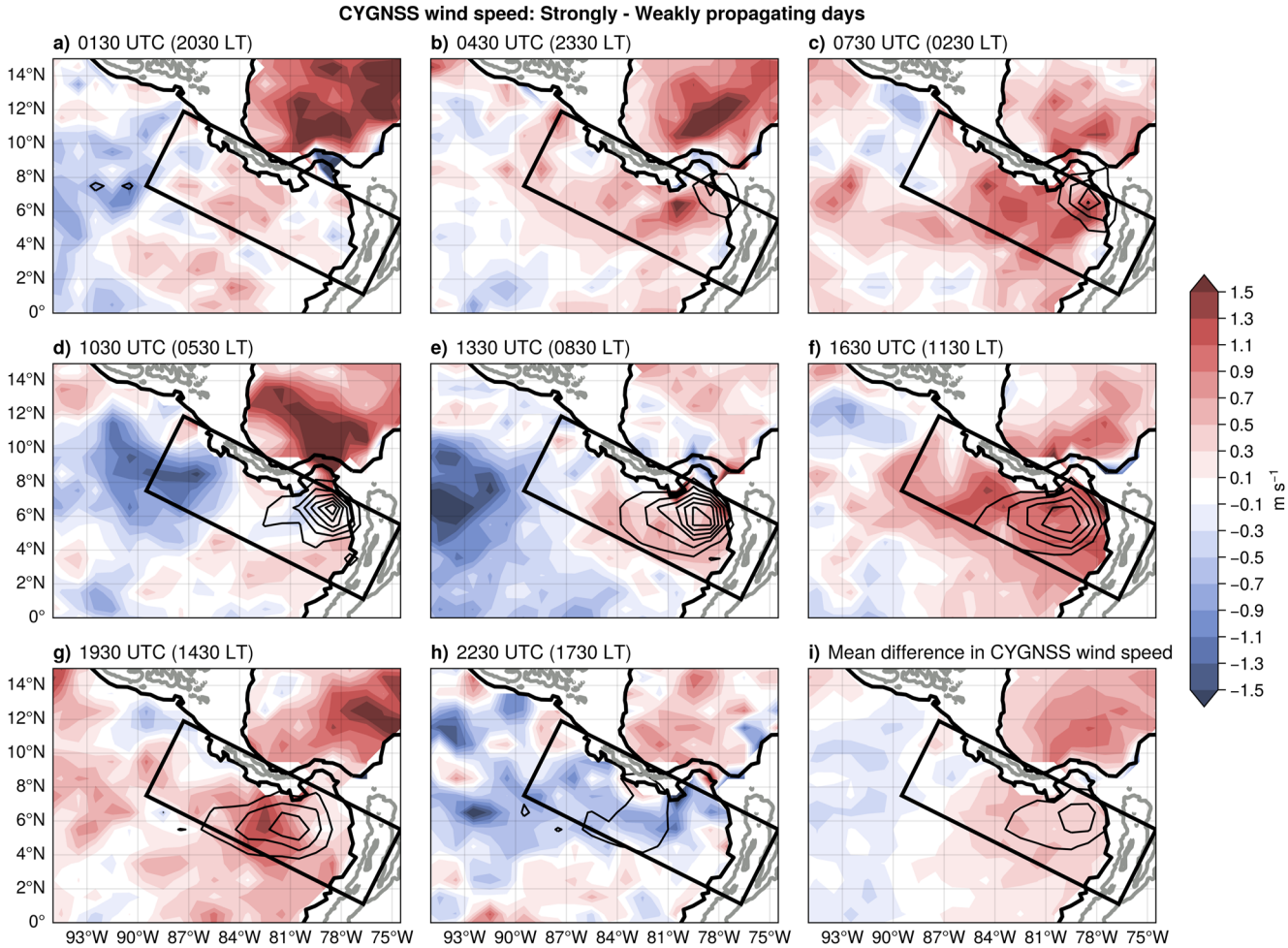

Figure 8. (a–h) Differences in three-hourly CYGNSS wind speed (shading) between the strongly and weakly propagating days with IMERG precipitation differences overlaid in black contours. (i) The average difference (i.e., the average of panels a–h) in CYGNSS wind speed (shading) and IMERG precipitation (contours). The precipitation contours start at 0.5 mm hr^{-1} and increment by 0.5 mm hr^{-1}. Gray contours represent the 1-km topography. The black rectangle indicates the region used to construct distance versus times plots in future figures.

air from the Caribbean (Figures 4 and 7a). The drying is partially offset by the VIMFC. A direct comparison of the energy in the atmospheric column lost due to precipitation versus the energy gained due to the VIMFC shows there is a deficit of 119 and 58 W m^{-2} in the far east Pacific (oceanic region inside the rectangle) during the strongly and weakly propagating days, respectively (not shown). LHFLXs help mitigate the energy deficit by contributing ∼100 W m^{-2} to the far east Pacific (oceanic region enclosed within the rectangle; 11c). One caveat to our comparison of VIMFC and precipitation is that we compared IMERG precipitation to ERA5 VIMFC and there are inconsistencies between the methods used to derive each product.

5. Discussion

Our results align well with previous studies of precipitation in the far east Pacific (i.e., Mejia et al., 2021; Zuluaga & Houze, 2015) that also found stronger regional circulations and moisture flux during days that had strong MCS activity. Tropics-wide, background winds, and moisture variability influence the ability of coastal precipitation to propagate offshore (Fang & Du, 2022). Fang and Du (2022) found that offshore propagation of diurnal tropical precipitation is highly favored in environments with sufficient moisture (>11 g kg^{-1}) and offshore or weak (<4 m s^{-1}) background winds. Their findings are consistent with observational studies for specific tropical regions such as southern China (Chen et al., 2019), the Philippines (Natoli & Maloney, 2019, 2023), and the MC region (e.g., Bai et al., 2021; Lu et al., 2019; Vincent & Lane, 2017). Numerical simulations also support

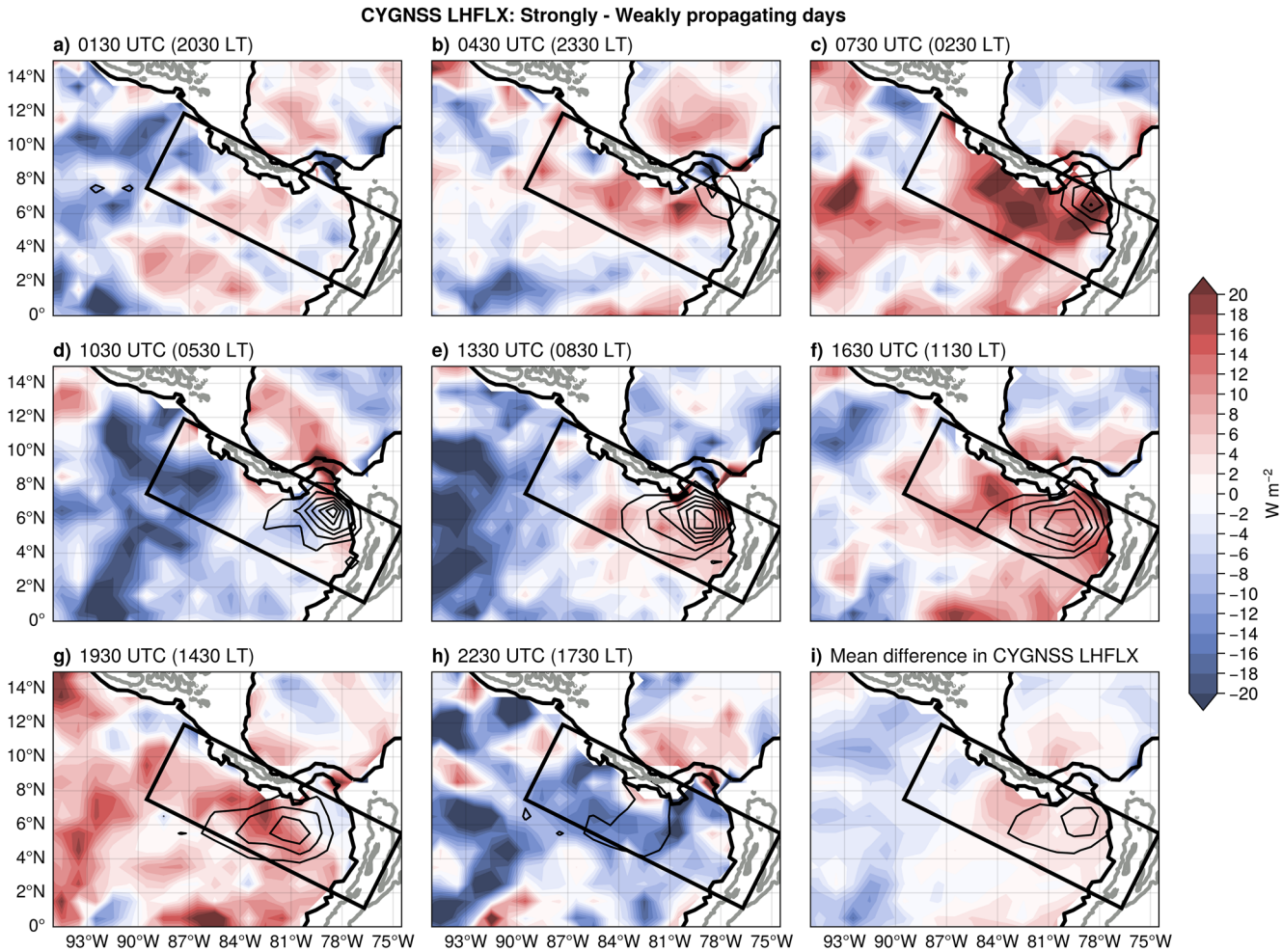

Figure 9. Same as Figure 8 except for CYGNSS-based latent heat flux (shading).

the importance of sufficient moisture (e.g., Coppin & Bellon, 2019) and offshore or weak winds (e.g., Wei & Pu, 2022) for the offshore propagation of diurnal tropical precipitation.

Collectively, the enhanced VIMFC, surface convergence, and wind-induced LHFLX associated with a stronger Choco Jet, CCLJ, and gap winds help increase moisture in the far east Pacific and encourage longer lasting precipitation and further westward propagation during the strongly propagating days. Figure 10 shows distance versus time plots of precipitation averaged over the width of the rectangle in previous figures overlaid with CYGNSS wind speed and LHFLX and ERA5 VIMFC and 1,000-600 hPa moisture. These plots summarize the relationship between the regional-scale environment and precipitation during the strongly versus weakly propagating days. During the strongly propagating days, offshore precipitation is heavier and extends further offshore than during the weakly propagating days (Figure 10). Enhanced wind speeds occur in the far east Pacific during most hours of the day during the strongly propagating days (Figure 10a) due to a stronger Choco Jet and gap winds. The enhanced winds promote stronger LHFLX and VIMFC (Figures 10b and 10c), which in turn support a more moist offshore environment both ahead of and before precipitation as well as during the enhanced precipitation (Figure 10d). As noted for Figures 8 and 9, a semidiurnal cycle is visible in the CYGNSS wind speed and LHFLX differences. The negative differences at 05:30 and 17:30 LT (10:30 and 22:30 UTC) roughly correspond to the semidiurnal peaks in zonal winds in the east Pacific (Ueyama & Deser, 2008).

Given that the differences in the offshore environment including moisture, winds, and fluxes are persistent throughout the day and consistent across the far east Pacific (Figure 11), we propose that changes in the background moisture, VIMFC, winds, and LHFLX, as opposed to differences in diurnal variations help explain the

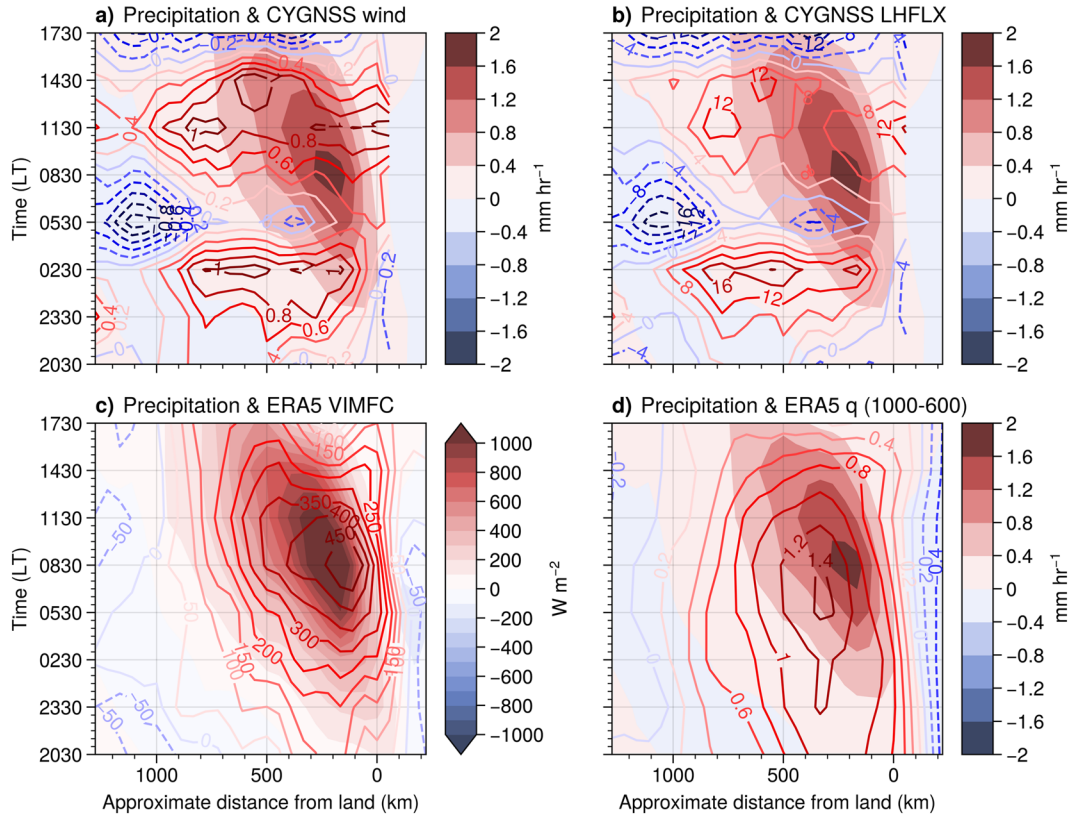

Figure 10. Distance versus time plots of diurnal cycle differences in IMERG precipitation (shading in each panel) in units of mm hr^{-1} in all panels except (c), which shows energy units of W m^{-2}. The contour lines represent differences in (a) CYGNSS wind speed (m s^{-1}), (b) CYGNSS LHFLX (W m^{-2}), (c) ERA5 vertically integrated moisture flux convergence (W m^{-2}) from 1,000 to 100 hPa, and (d) mass-weighted vertically integrated (1,000-600 hPa) specific humidity (kg m^{-2}). Differences were calculated by averaging over the width (i.e., short side) of the rectangle. The *x*-axis represents the approximate distance from the Colombian coast along the length (i.e., long side) of the rectangle in previous figures.

degree to which diurnal precipitation can propagate westward in the far east Pacific. To ensure that changes in the background environment actually support the extended offshore propagation of precipitation during the strongly propagating days and not merely any offshore precipitation (i.e., precipitation originating offshore), we examined the environmental conditions during days that only had precipitation originating offshore (i.e., PC2 > 1 and PC1 < 1). Similar to the strongly propagating days, the offshore-precipitation days had enhanced moisture associated with an increased Choco Jet and CLLJ and enhanced convergence, VIMFC, and vorticity. However, the enhancements during the offshore days are not as strong nor as pervasive as during the strongly propagating days. Rather, the enhanced moisture, convergence, vorticity, and VIMFC are focused several hundred kilometers from the Colombian coast between 5°N and 7°N and west 80°W. Closer to the coast, the offshore days generally have reduced moisture and offshore winds associated with divergence and weaker VIMFC and vorticity relative to both the weakly and strongly propagating days (not shown). Therefore, the nearshore environmental conditions seem especially important for dictating the ability of precipitation to propagate offshore.

Specific mechanisms that generate the westward-propagation of precipitation, such as land breezes and gravity waves discussed in the introduction, were not analyzed in this paper. However, we speculate that in the nearshore environment (<150 km) density currents generated by land breezes overnight or cold pools at least partially explain the westward propagation of precipitation during both the strongly and weakly propagating days. The propagation speed of the precipitation in the nearshore environment is roughly 8 and 5 m s^{-1} during the strongly and weakly propagating days (Figure 3), respectively, which is close to the characteristic range of density currents (i.e., 3–7 m s^{-1}; Fang & Du, 2022). Further from the coast, gravity waves likely help to move the precipitation westward. During the strongly propagating days, the propagation speed increases to about 12 m s^{-1} 150 km off the coast, consistent with the findings of Mapes, Warner, Xu, et al. (2003), Mapes, Warner, & Xu (2003), Warner

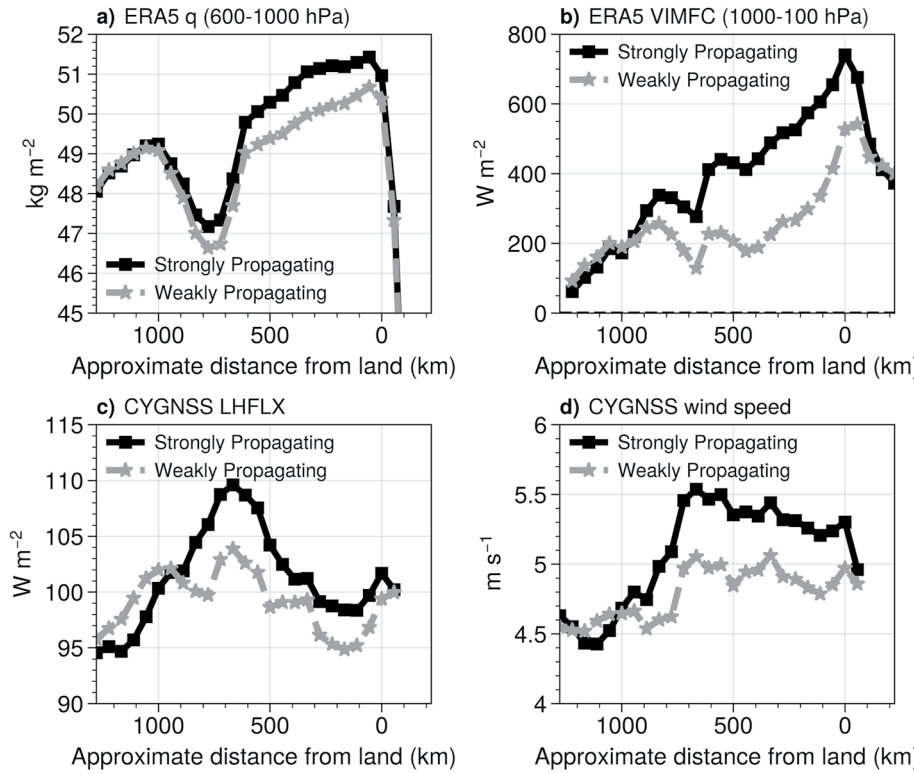

Figure 11. ERA5 (a) mass-weighted specific humidity integrated from 1,000 to 600 hPa and (b) vertically integrated moisture flux convergence integrated from 1,000 to 100 hPa averaged over all times of the day and the width (i.e., short side) of the rectangle for the strongly (black line) and weakly propagating (gray line) days. (c) and (d) are the same as (a) and (b), except for CYGNSS LHFLX and wind speed, respectively. The *x*-axis represents the approximate distance from the Colombian coast along the long side of the rectangle in previous figures.

et al. (2003), and Yepes et al. (2020) who attributed similar offshore propagation speeds to gravity-wave dynamics. Gravity waves may also be initiated over land during the weakly propagating days; however, we hypothesize that as the wave propagates offshore the background moisture is insufficient to sustain the precipitation. By contrast, during the strongly propagating days sufficient moisture sustains convection generated by the instability of gravity waves. This hypothesis aligns with previous studies that found that the offshore propagation of precipitation throughout the tropics is mainly driven by density currents near the coast and gravity waves far from the coast (e.g., Bai et al., 2021; Fang & Du, 2022; Short et al., 2019; Vincent & Lane, 2016).

The atmospheric conditions preceding the strongly propagating days may also influence the enhanced moisture during the strongly propagating days. A lack of convective activity on the preceding day could allow moisture to build up and make conditions more favorable for convection the next day. This 2-day cycle of convection was observed during TOGA COARE (Chen & Houze, 1997) and is hinted at here for the east Pacific (Figure 1c). Future work is needed to determine how influential the prior day's convective inactivity is for ripening the environmental conditions for strong diurnal westward propagation in the far east Pacific.

To further demonstrate the importance of the background as opposed to diurnal variations, Figure 12 shows that diurnal anomalies of wind speed, LHFLX, and moisture during the strongly and weakly propagating days. The diurnal anomalies were calculated independently for each subset of days by removing the daily mean of each variable from the hourly composites for the strongly and weakly propagating days separately. By calculating the diurnal anomalies for the strongly and weakly propagating days separately, we can compare differences in the amplitude of diurnal variations during the two subsets of days. The weakly propagating days, actually have stronger diurnal variations (or amplitude) in wind speed, LHFLX, and moisture despite having weaker diurnal variations in precipitation (Figure 12). The weakly propagating days also have a robust semidiurnal cycle in wind speed and LHFLX that peak at 05:30 and 17:30 LT and correspond to the peaks in the semidiurnal cycle of zonal wind in the east Pacific related to semidiurnal cycle of the solar tide (Ueyama & Deser, 2008). Further analysis,

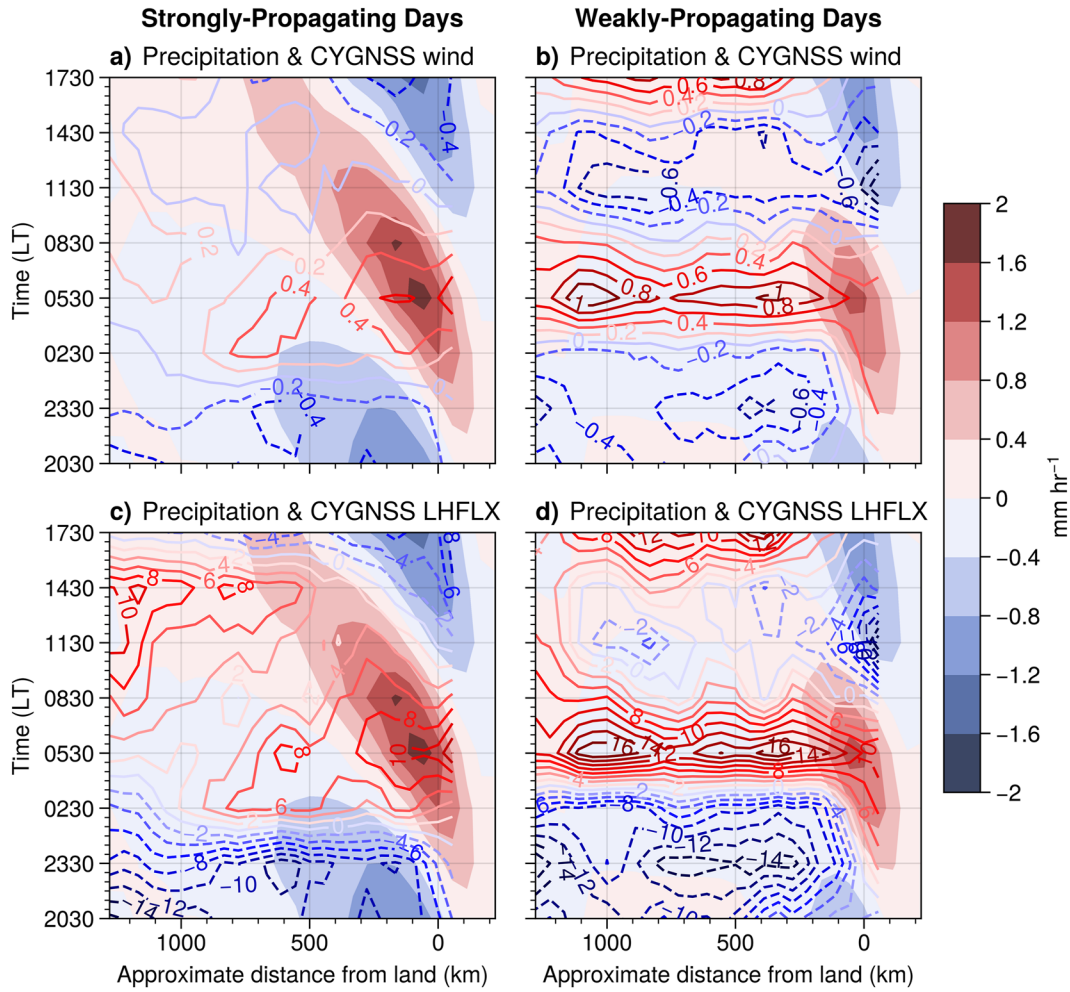

Figure 12. Distance versus time plots of diurnal cycle anomalies of IMERG precipitation (shading) and CYGNSS wind speed (contours in m s^{-1}) during (a) strongly and (b) weakly propagating days. (c) and (d) are the same as (a) and (b), except the contours represent diurnal cycle anomalies in CYGNSS LHFLX (W m^{-2}). The *x*-axis represents the approximate distance from the Colombian coast along the long side of the rectangle in previous figures.

which is beyond this scope of this current work, would be necessary to diagnose why the weakly propagating days show a robust semidiurnal cycle, while the strongly propagating days do not.

The results in Figure 12 and previous figures suggest that the westward-propagating precipitation in the far east Pacific is more sensitive to its background environment than to the strength of diurnal fluctuations, since the strongly propagating days have increased moisture and regional circulations (Figures 4–11) but weaker diurnal-cycle variations (Figure 12). The stronger diurnal cycle of wind speeds during the weakly propagating days is contrary to that found during the OTREC period, when diurnal variations in wind speeds at Nuqui, Colombia were stronger for wet days than dry days (Mejia et al., 2021). The contrasting observations may stem from the Nuqui results being based on comparisons of only 00 and 12 UTC soundings as opposed to all hours of the day. Additionally, our strongly and weakly propagating days are defined differently than Mejia et al.'s (2021) wet versus dry days (discussed in Section 1).

6. Summary and Conclusion

This work examined physical mechanisms that contribute to a strong diurnal cycle of precipitation along the coast of Colombia and into the far east Pacific. Diurnal convection is frequently initiated over the western slopes of the Andes mountains in Colombia during the late afternoon and then moves westward toward the coast and

offshore overnight. As the convection moves offshore, it often develops into MCSs. These MCSs can then seed EWs, which may develop into TCs.

To determine what environmental factors contribute to a strong diurnal cycle of westward propagating precipitation in the far east Pacific, we developed an index based on the leading two EOFs of IMERG precipitation that identifies days with strongly or weakly propagating precipitation. Composites of ERA5 wind and specific humidity revealed that days with strongly propagating diurnal precipitation have stronger regional circulations including the Choco Jet, the CLLJ, and enhanced gap winds including the Papagayo and Panama Jets. Accompanying these stronger flows is enhanced moisture and vorticity throughout the Panama Bight. Increased precipitation during the strongly propagating days is also directly linked, through the moisture budget, to increases in VIMFC throughout the far east Pacific. These findings are consistent with previous work based on field campaign observations (i.e., Mejia et al., 2021) and satellite and reanalysis measurements (i.e., Zuluaga & Houze, 2015).

Unique to our work was the evaluation of surface wind speed observations from the CYGNSS microsatellites. We also analyzed the CYGNSS wind speed-based LHFLX product to determine the LHFLX contribution to diurnal precipitation in the Panama Bight that was notably missing from previous works (Mejia et al., 2021; Zuluaga & Houze, 2015). CYGNSS wind speeds were similar to ERA5 and showed a stronger Choco Jet and CLLJ and enhanced gap winds during most hours of the strongly propagating days. During the strongly propagating days, increases in LHFLX generally mimicked the wind speed enhancements and contributed to the increased moisture in the Panama Bight.

On strongly propagating days, stronger regional circulations and wind-induced LHFLX and MFC contribute to enhanced moisture and vorticity in the far east Pacific. This more favorable offshore environment sustains the westward propagation of diurnal precipitation beyond that observed during weakly propagating days. The environmental differences are generally consistent during all hours of the day, suggesting that differences in the background circulation and moisture field are more important than differences in their diurnal variations. To support this hypothesis, we showed that diurnal-cycle variations in CYGNSS wind speed and fluxes were actually stronger during the weakly propagating days as opposed to the strongly propagating days despite the strongly propagating days having increased offshore precipitation. A semidiurnal cycle in CYGNSS wind speeds and LHFLX during the weakly propagating days was also noted. We speculate that these semidiurnal peaks are related to the semidiurnal fluctuations of the solar tide. However, it is possible that the semidiurnal signal is a spurious artifact of CYGNSS data processing. The root cause of the semidiurnal signal is beyond the scope of this current work. Future work will further examine the importance of LHFLX to moisture variations and precipitation in the far east Pacific through mechanism denial experiments with regional cloud resolving models.

A natural question arising from this work is what causes the variations in the strength of the regional circulations, which then impact the moisture variations into the far east Pacific. Annual and interannual variations of the CCLJ and the associated gap winds and the Choco Jet have been linked to variations in the El Nino Southern Oscillation (ENSO; e.g., Arias et al., 2015; Hoyos et al., 2019; Morales et al., 2021; Poveda & Mesa, 2000; Poveda et al., 2006, 2011; Sierra et al., 2021) and the MJO (e.g., Maloney & Hartmann, 2001; Serra et al., 2010), respectively. Further, the CLLJ is to first-order geostrophically driven and therefore strongly influenced seasonally by the westward extent of the North Atlantic subtropical high (e.g., Cook & Vizy, 2010; Wang, 2007). There is very little work discussing the fluctuations of these regional jets at the synoptic timescale. One source of variability may be EWs (Rydbeck et al., 2017; Serra et al., 2010). Mejia et al. (2021) also mention EW as a source of variability in the CLLJ during the days identified as wet versus dry. García-Martínez and Bollasina (2020) further discuss a link between fluctuations in extratropical waves to variations in the strength of the CCLJ, which may be important to the variations we have discussed here. Determining the cause of the variability in the regional circulations that we have found here is worthy of a future investigation.

Data Availability Statement

The CYGNSS wind Science Data Record, version 3.1 (CYGNSS, 2021), and flux Science Data Record, version 2.0 (CYGNSS, 2022), data files are distributed through the NASA's Physical Oceanography Distributed Active Archive Center (PO.DAAC) (https://podaac.jpl.nasa.gov/CYGNSS). ERA5 data (Hersbach et al., 2018a, 2018b) were downloaded from the Copernicus Climate Change Service (C3S) Climate Data Store. The results contain modified Copernicus Climate Change Service information 2021–2022. Neither the European Commission nor

ECMWF is responsible for any use that may be made of the Copernicus information or data it contains. The GPM IMERG data (Huffman, Stocker, et al., 2019) were provided by the NASA/Goddard Space Flight Center's Precipitation Processing Center, which develop and compute the GPM IMERG data as a contribution to GPM, and archived at the NASA GES DISC (https://disc.gsfc.nasa.gov). The plots were made using the Python matplotlib wrapper ProPlot (https://doi.org/10.5281/zenodo.5602155) created by Luke Davis.

Acknowledgments

We are grateful to Hien Bui for feedback on this work and Isla Simpson for use of her python code to compute the vertically integrated MFC for ERA5. We are grateful for the comments from Prof. Naoko Sakaeda and two anonymous reviewers, which helped to improve this paper. Emily Riley Dellaripa and Eric Maloney were supported by the NASA CYGNSS, under Grant 80NSSC21K1004. Eric Maloney was additionally supported by the NSF Climate and Large-Scale Dynamics, under Grants AGS-1735978 and AGS-2217785. Charlotte DeMott was supported by the NOAA Climate Variability and Predictability, under Grant NA20OAR4310374 and DOE Regional and Global Model Analysis, under Grant DE-SC0020092.

References

Amador, J. A. (1998). A climatic feature of the tropical Americas: The trade wind easterly jet. *Topicos Meteorologicos y Oceanograficos*, *5*(2), 91–102.

Amador, J. A., Alfaro, E. J., Lizano, O. G., & Magaña, V. O. (2006). Atmospheric forcing of the eastern tropical Pacific: A review. *Progress in Oceanography*, *69*(2–4), 101–142. https://doi.org/10.1016/j.pocean.2006.03.007

Araligidad, N. M., & Maloney, E. D. (2008). Wind-driven latent heat flux and the intraseasonal oscillation. *Geophysical Research Letters*, *35*, L04815. https://doi.org/10.1029/2007GL032746

Arias, P. A., Martínez, J. A., & Vieira, S. C. (2015). Moisture sources to the 2010–2012 anomalous wet season in northern South America. *Climate Dynamics*, *45*(9), 2861–2884. https://doi.org/10.1007/s00382-015-2511-7

Asharaf, S., Posselt, D. J., Said, F., & Ruf, C. S. (2022). Updates on CYGNSS ocean surface wind validation in the tropics. *Journal of Atmospheric and Oceanic Technology*, *40*(1), 37–51. https://doi.org/10.1175/JTECH-D-21-0168.1

Bai, H., Deranadyan, G., Schumacher, C., Funk, A., Epifanio, C., Ali, A., et al. (2021). Formation of nocturnal offshore rainfall near the West Coast of Sumatra: Land breeze or gravity wave? *Monthly Weather Review*, *149*(3), 715–731. https://doi.org/10.1175/mwr-d-20-0179.1

Balasubramaniam, R., & Ruf, C. (2020). Characterization of rain impact on L-band GNSS-R ocean surface measurements. *Remote Sensing of Environment*, *239*, 111607. https://doi.org/10.1016/j.rse.2019.111607

Bui, H. X., Maloney, E. D., Riley Dellaripa, E. M., & Singh, B. (2020). Wind speed, surface flux, and intraseasonal convection coupling from CYGNSS data. *Geophysical Research Letters*, *47*, e2020GL090376. https://doi.org/10.1029/2020GL090376

Chelton, D. B., Freilich, M. H., & Esbensen, S. K. (2000). Satellite observations of the wind jets off the Pacific coast of central America. Part I: Case studies and statistical characteristics. *Monthly Weather Review*, *128*(7), 1993–2018. https://doi.org/10.1175/1520-0493(2000)128<1993:sootwj>2.0.co;2

Chen, S. S., & Houze, R. A., Jr. (1997). Diurnal variation and life-cycle of deep convective systems over the tropical Pacific warm pool. *Quarterly Journal of the Royal Meteorological Society*, *123*(538), 357–388. https://doi.org/10.1002/qj.49712353806

Chen, X., Zhang, F., & Ruppert, J. H. (2019). Modulations of the diurnal cycle of coastal rainfall over South China caused by the boreal summer intraseasonal oscillation. *Journal of Climate*, *32*(7), 2089–2108. https://doi.org/10.1175/JCLI-D-18-0786.1

Cook, K. H., & Vizy, E. K. (2010). Hydrodynamics of the Caribbean low-level jet and its relationship to precipitation. *Journal of Climate*, *23*(6), 1477–1494. https://doi.org/10.1175/2009jcli3210.1

Coppin, D., & Bellon, G. (2019). Physical mechanisms controlling the offshore propagation of convection in the tropics: 1. Flat Island. *Journal of Advances in Modeling Earth Systems*, *11*, 3042–3056. https://doi.org/10.1029/2019MS001793

Crespo, J. A., Posselt, D. J., & Asharaf, S. (2019). CYGNSS surface heat flux product development. *Remote Sensing*, *11*(19), 2294. https://doi.org/10.3390/rs11192294

CYGNSS. (2021). CYGNSS Level 2 Science Data Record Version 3.1. Ver. 3.1 [Dataset]. PO.DAAC. https://doi.org/10.5067/CYGNS-L2X31

CYGNSS. (2022). CYGNSS Level 2 Ocean Surface Heat Flux Science Data Record Version 2.0. Ver. 2.0 [Dataset]. PO.DAAC. https://doi.org/10.5067/CYGNS-L2H20

Dai, A., & Wang, J. (1999). Diurnal and semidiurnal tides in global surface pressure fields. *Journal of the Atmospheric Sciences*, *56*(22), 3874–3891. https://doi.org/10.1175/1520-0469(1999)056<3874:DASTIG>2.0.CO;2

DeMott, C. A., Benedict, J. J., Klingaman, N. P., Woolnough, S. J., & Randall, D. A. (2016). Diagnosing ocean feedbacks to the MJO: SST-modulated surface fluxes and the moist static energy budget. *Journal of Geophysical Research: Atmospheres*, *121*, 8350–8373. https://doi.org/10.1002/2016JD025098

DeMott, C. A., Klingaman, N. P., & Woolnough, S. J. (2015). Atmosphere-ocean coupled processes in the Madden-Julian oscillation. *Reviews of Geophysics*, *53*, 1099–1154. https://doi.org/10.1002/2014RG000478

DeMott, C. A., Stan, C., Randall, D. A., & Branson, M. D. (2014). Intraseasonal variability in coupled GCMs: The roles of ocean feedbacks and model physics. *Journal of Climate*, *27*(13), 4970–4995. https://doi.org/10.1175/jcli-d-13-00760.1

DeMott, C. A., Wolding, B. O., Maloney, E. D., & Randall, D. A. (2018). Atmospheric mechanisms for MJO decay over the maritime continent. *Journal of Geophysical Research: Atmospheres*, *123*, 5188–5204. https://doi.org/10.1029/2017JD026979

Deser, C., & Smith, C. A. (1998). Diurnal and semidiurnal variations of the surface wind field over the tropical Pacific Ocean. *Journal of Climate*, *11*(7), 1730–1748. https://doi.org/10.1175/1520-0442(1998)011<1730:DASVOT>2.0.CO;2

Edson, J. B., Jampana, V., Weller, R. A., Bigorre, S. P., Plueddemann, A. J., Fairall, C. W., et al. (2013). On the exchange of momentum over the open ocean. *Journal of Physical Oceanography*, *43*(8), 1589–1610. https://doi.org/10.1175/jpo-d-12-0173.1

Fairall, C. W., Bradley, E. F., Hare, J. E., Grachev, A. A., & Edson, J. B. (2003). Bulk parameterization of air-sea fluxes: Updates and verification for the COARE algorithm. *Journal of Climate*, *16*(4), 571–591. https://doi.org/10.1175/1520-0442(2003)016<0571:BPOASF>2.0.CO2

Fang, J., & Du, Y. (2022). A global survey of diurnal offshore propagation of rainfall. *Nature Communications*, *13*(1), 7437. https://doi.org/10.1038/s41467-022-34842-0

Fuchs-Stone, Ž., Raymond, D. J., & Sentić, S. (2020). OTREC2019: Convection over the east Pacific and southwest Caribbean. *Geophysical Research Letters*, *47*, e2020GL087564. https://doi.org/10.1029/2020GL087564

García-Martínez, I. M., & Bollasina, M. A. (2020). Sub-monthly evolution of the Caribbean low-level jet and its relationship with regional precipitation and atmospheric circulation. *Climate Dynamics*, *54*(9), 4423–4440. https://doi.org/10.1007/s00382-020-05237-y

Garreaud, R., & Wallace, J. M. (1997). The diurnal march of convective cloudiness over the Americas. *Monthly Weather Review*, *125*(12), 3157–3171. https://doi.org/10.1175/1520-0493(1997)125<3157:tdmocc>2.0.co;2

Gentine, P., Garelli, A., Park, S., Nie, J., Torri, G., & Kuang, Z. (2016). Role of surface heat fluxes underneath cold pools. *Geophysical Research Letters*, *43*, 874–883. https://doi.org/10.1002/2015GL067262

Hassim, M. E. E., Lane, T. P., & Grabowski, W. W. (2016). The diurnal cycle of rainfall over New Guinea in convection-permitting WRF simulations. *Atmospheric Chemistry and Physics*, *16*(1), 161–175. https://doi.org/10.5194/acp-16-161-2016

Hastenrath, S. (2002). The intertropical convergence zone of the eastern Pacific revisited. *International Journal of Climatology*, *22*(3), 347–356. https://doi.org/10.1002/joc.739

Hendon, H. (2005). Air-sea interaction. In W. K. M. Lau, & D. E. Waliser (Eds.), *Intraseasonal variability in the atmosphere-ocean climate system* (pp. 223–246). Springer.

Hersbach, H., Bell, B., Berrisford, P., Biavati, G., Horányi, A., Muñoz Sabater, J., et al. (2018a). ERA5 hourly data on pressure levels from 1959 to present [Dataset]. Copernicus Climate Change Service (C3S) Climate Data Store (CDS). https://doi.org/10.24381/cds.bd0915c6

Hersbach, H., Bell, B., Berrisford, P., Biavati, G., Horányi, A., Muñoz Sabater, J., et al. (2018b). ERA5 hourly data on single levels from 1959 to present [Dataset]. Copernicus Climate Change Service (C3S) Climate Data Store (CDS). https://doi.org/10.24381/cds.adbb2d47

Hersbach, H., Bell, B., Berrisford, P., Hirahara, S., Horányi, A., Muñoz-Sabater, J., et al. (2020). The ERA5 global reanalysis. *Quarterly Journal of the Royal Meteorological Society*, *146*(730), 1999–2049. https://doi.org/10.1002/qj.3803

Ho, C.-H., Park, M.-S., Choi, Y.-S., & Takayabu, Y. N. (2008). Relationship between intraseasonal oscillation and diurnal variation of summer rainfall over the South China Sea. *Geophysical Research Letters*, *35*, L03701. https://doi.org/10.1029/2007GL031962

Holloway, C. E., & Woolnough, S. J. (2016). The sensitivity of convective aggregation to diabatic processes in idealized radiative-convective equilibrium simulations. *Journal of Advances in Modeling Earth Systems*, *8*, 166–195. https://doi.org/10.1002/2015MS000511

Houze, R. A. (2012). Orographic effects on precipitating clouds. *Reviews of Geophysics*, *50*, RG1001. https://doi.org/10.1029/2011RG000365

Houze, R. A., Jr., Geotis, S. G., Marks, F. D., Jr., & West, A. K. (1981). Winter monsoon convection in the vicinity of north Borneo. Part I: Structure and time variation of the clouds and precipitation. *Monthly Weather Review*, *109*(8), 1595–1614. https://doi.org/10.1175/1520-0493(1981)109<1595:wmcitv>2.0.co;2

Hoyos, I., Cañón-Barriga, J., Arenas-Suárez, T., Dominguez, F., & Rodríguez, B. A. (2019). Variability of regional atmospheric moisture over Northern South America: Patterns and underlying phenomena. *Climate Dynamics*, *52*(1), 893–911. https://doi.org/10.1007/s00382-018-4172-9

Huffman, G. J., Bolvin, D. T., Braithwaite, D., Hsu, K., Joyce, R., Kidd, C., et al. (2019a). NASA Global Precipitation Measurement (GPM) Integrated Multi-satellitE Retrievals for GPM (IMERG), NASA algorithm theoretical basis document (ATBD), version 6.0. Retrieved from https://docserver.gesdisc.eosdis.nasa.gov/public/project/GPM/IMERG_ATBD_V06.pdf

Huffman, G. J., Stocker, E. F., Bolvin, D. T., Nelkin, E. J., & Tan, J. (2019b). GPM IMERG Final Precipitation L3 Half Hourly 0.1 degree x 0.1 degree V06 [Dataset]. Goddard Earth Sciences Data and Information Services Center (GES DISC). https://doi.org/10.5067/GPM/IMERG/3B-HH/06

Jaramillo, L., Poveda, G., & Mejía, J. F. (2017). Mesoscale convective systems and other precipitation features over the tropical Americas and surrounding seas as seen by TRMM. *International Journal of Climatology*, *37*(S1), 380–397. https://doi.org/10.1002/joc.5009

Kerns, B., Greene, K., & Zipser, E. (2008). Four years of tropical ERA-40 vorticity maxima tracks. Part I: Climatology and vertical vorticity structure. *Monthly Weather Review*, *136*(11), 4301–4319. https://doi.org/10.1175/2008mwr2390.1

Kirshbaum, J. D., Adler, B., Kalthoff, N., Barthlott, C., & Serafin, S. (2018). Moist orographic convection: Physical mechanisms and links to surface-exchange processes. *Atmosphere*, *9*(3), 80. https://doi.org/10.3390/atmos9030080

Kohyama, T., & Wallace, J. M. (2016). Rainfall variations induced by the lunar gravitational atmospheric tide and their implications for the relationship between tropical rainfall and humidity. *Geophysical Research Letters*, *43*, 918–923. https://doi.org/10.1002/2015GL067342

Lu, J., Li, T., & Wang, L. (2019). Precipitation diurnal cycle over the maritime continent modulated by the MJO. *Climate Dynamics*, *53*(9), 6489–6501. https://doi.org/10.1007/s00382-019-04941-8

Maloney, E. D., & Hartmann, D. L. (2001). The Madden-Julian Oscillation, barotropic dynamics, and north Pacific tropical cyclone formation. Part I: Observations. *Journal of the Atmospheric Sciences*, *58*(17), 2545–2558. https://doi.org/10.1175/1520-0469(2001)058<2545:TMJOBD>2.0.CO;2

Mapes, B. E., Warner, T. T., & Xu, M. (2003). Diurnal patterns of rainfall in northwestern South America. Part III: Diurnal gravity waves and nocturnal convection offshore. *Monthly Weather Review*, *131*(5), 830–844. https://doi.org/10.1175/1520-0493(2003)131<0830:dporin>2.0.co;2

Mapes, B. E., Warner, T. T., Xu, M., & Negri, A. J. (2003). Diurnal patterns of rainfall in northwestern South America. Part I: Observations and context. *Monthly Weather Review*, *131*(5), 799–812. https://doi.org/10.1175/1520-0493(2003)131<0799:dporin>2.0.co;2

Mejía, J. F., & Poveda, G. (2005). Ambientes atmosféricos de sistemas convectivos de mesoescala sobre Colombia durante 1998 según la misión TRMM y el re-análisis NCEP/NCAR. *Revista de la Academia Colombiana de Ciencias Exactas*, *29*(113), 495–514.

Mejía, J. F., Yepes, J., Henao, J. J., Poveda, G., Zuluaga, M. D., Raymond, D. J., & Fuchs-Stone, Ž. (2021). Towards a mechanistic understanding of precipitation over the far eastern tropical Pacific and Western Colombia, one of the rainiest spots on Earth. *Journal of Geophysical Research: Atmospheres*, *126*, e2020JD033415. https://doi.org/10.1029/2020JD033415

Morales, J. S., Arias, P. A., Martínez, J. A., & Durán-Quesada, A. M. (2021). The role of low-level circulation on water vapour transport to central and northern South America: Insights from a 2D Lagrangian approach. *International Journal of Climatology*, *41*(S1), E2662–E2682. https://doi.org/10.1002/joc.6873

Murphy, R. C. (1939). The littoral of Pacific Colombia and Eduador. *Geographical Review*, *29*(1), 1–33. https://doi.org/10.2307/210063

Natoli, M. B., & Maloney, E. D. (2019). Intraseasonal variability of the diurnal cycle of precipitation in the Philippines. *Journal of the Atmospheric Sciences*, *76*(11), 3633–3654. https://doi.org/10.1175/jas-d-19-0152.1

Natoli, M. B., & Maloney, E. D. (2023). The tropical diurnal cycle under varying states of the monsoonal background wind. *Journal of the Atmospheric Sciences*, *80*(1), 235–258. https://doi.org/10.1175/JAS-D-22-0045.1

Negri, A. J., Anagnostou, E. N., & Adler, R. F. (2000). A 10-yr climatology of Amazonian rainfall derived from passive microwave satellite observations. *Journal of Applied Meteorology*, *39*(1), 42–56. https://doi.org/10.1175/1520-0450(2000)039<0042:aycoar>2.0.co;2

Nichols, J. T., & Murphy, R. C. (1944). A collection of fishes from the Panama Bight, Pacific Ocean. *Bulletin of the American Museum of Natural History*, *83*, 217–260.

Park, M.-S., Ho, C.-H., Kim, J., & Elsberry, R. L. (2011). Diurnal circulations and their multi-scale interaction leading to rainfall over the South China Sea upstream of the Philippines during intraseasonal monsoon westerly wind bursts. *Climate Dynamics*, *37*(7), 1483–1499. https://doi.org/10.1007/s00382-010-0922-z

Pascual, D., Clarizia, M. P., & Ruf, C. S. (2021). Improved CYGNSS wind speed retrieval using significant wave height correction. *Remote Sensing*, *13*(21), 4313. https://doi.org/10.3390/rs13214313

Pascual, D., Clarizia, M. P., Zavorotny, V., McKague, D., & Ruf, C. (2021). Level 2 wind speed retrieval UM Doc. No. 148-0138 SwRI Doc. No. N/A R. Rev. 7. Retrieved from https://archive.podaac.earthdata.nasa.gov/podaac-ops-cumulus-docs/cygnss/open/L2/docs/148-0138_ATBD_L2_Wind_Speed_Retrieval_R7.pdf

Poveda, G., Álvarez, D. M., & Rueda, Ó. A. (2011). Hydro-climatic variability over the Andes of Colombia associated with ENSO: A review of climatic processes and their impact on one of the Earth's most important biodiversity hotspots. *Climate Dynamics*, *36*(11), 2233–2249. https://doi.org/10.1007/s00382-010-0931-y

Poveda, G., Jaramillo, L., & Vallejo, L. F. (2014). Seasonal precipitation patterns along pathways of South American low-level jets and aerial rivers. *Water Resources Research*, *50*, 98–118. https://doi.org/10.1002/2013WR014087

Poveda, G., & Mesa, O. J. (1999). The westerly low-level Chocó jet and two other atmospheric jets over Colombia: Climatology and variability during ENSO phases (in Spanish). *Academia Colombiana de Ciencias Exactas, Fisicas Y Naturales. Revista*, *23*, 517–528.
Poveda, G., & Mesa, O. J. (2000). On the existence of Lloró (the rainiest locality on Earth): Enhanced ocean-land-atmosphere interaction by a low-level jet. *Geophysical Research Letters*, *27*, 1675–1678. https://doi.org/10.1029/1999GL006091
Poveda, G., Mesa, O. J., Salazar, L. F., Arias, P. A., Moreno, H. A., Vieira, S. C., et al. (2005). The diurnal cycle of precipitation in the tropical Andes of Colombia. *Monthly Weather Review*, *133*(1), 228–240. https://doi.org/10.1175/mwr-2853.1
Poveda, G., Waylen, P. R., & Pulwarty, R. S. (2006). Annual and inter-annual variability of the present climate in northern South America and southern Mesoamerica. *Palaeogeography, Palaeoclimatology, Palaeoecology*, *234*(1), 3–27. https://doi.org/10.1016/j.palaeo.2005.10.031
Qian, J.-H. (2008). Why precipitation is mostly concentrated over Islands in the maritime continent. *Journal of the Atmospheric Sciences*, *65*(4), 1428–1441. https://doi.org/10.1175/2007jas2422.1
Redelsperger, J., Guichard, F., & Mondon, S. (2000). A parameterization of mesoscale enhancement of surface fluxes for large-scale models. *Journal of Climate*, *13*(2), 402–421. https://doi.org/10.1175/1520-0442(2000)013<0402:APOMEO>2.0.CO;2
Riley Dellaripa, E. M., Maloney, E., & van den Heever, S. C. (2018). Wind-flux feedbacks and convective organization during the November 2011 MJO event in a high-resolution model. *Journal of the Atmospheric Sciences*, *75*(1), 57–84. https://doi.org/10.1175/jas-d-16-0346.1
Riley Dellaripa, E. M., & Maloney, E. D. (2015). Analysis of MJO wind-flux feedbacks in the Indian Ocean using RAMA buoy observations. *Journal of the Meteorological Society of Japan. Series II*, *93A*, 1–20. https://doi.org/10.2151/jmsj.2015-021
Riley Dellaripa, E. M., Maloney, E. D., Toms, B. A., Saleeby, S. M., & van den Heever, S. C. (2020). Topographic effects on the Luzon diurnal cycle during the BSISO. *Journal of the Atmospheric Sciences*, *77*(1), 3–30. https://doi.org/10.1175/jas-d-19-0046.1
Ruf, C., Asharaf, S., Balasubramaniam, R., Gleason, S., Lang, T., McKague, D., et al. (2019). In-orbit performance of the constellation of CYGNSS Hurricane satellites. *Bulletin of the American Meteorological Society*, *100*(10), 2009–2023. https://doi.org/10.1175/bams-d-18-0337.1
Ruf, C. S. (2018). Algorithm theoretical basis document. Level 3 gridded wind speed. CYGNSS project document, 148-0319, Rev 1, 20 Aug. 2018.
Ruf, C. S., Atlas, R., Chang, P. S., Clarizia, M. P., Garrison, J. L., Gleason, S., et al. (2016). New Ocean winds satellite mission to probe hurricanes and tropical convection. *Bulletin of the American Meteorological Society*, *97*(3), 385–395. https://doi.org/10.1175/bams-d-14-00218.1
Ruf, C. S., & Balasubramaniam, R. (2019). Development of the CYGNSS geophysical model function for wind speed. *IEEE Journal of Selected Topics in Applied Earth Observations and Remote Sensing*, *12*(1), 66–77. https://doi.org/10.1109/JSTARS.2018.2833075
Ruf, C. S., & Twigg, D. (2020). CYGNSS level 1 and 2 trackwise corrected climate data record (Rev. *1*). Retrieved from https://podaac-tools.jpl.nasa.gov/drive/files/allData/cygnss/L2/docs/148-0389-1_ATBD_Trackwise_Corrected_CDR.pdf
Rydbeck, A. V., & Maloney, E. D. (2015). On the convective coupling and moisture organization of east Pacific easterly waves. *Journal of the Atmospheric Sciences*, *72*(10), 3850–3870. https://doi.org/10.1175/jas-d-15-0056.1
Rydbeck, A. V., Maloney, E. D., & Alaka, G. J., Jr. (2017). In situ initiation of east Pacific easterly waves in a regional model. *Journal of the Atmospheric Sciences*, *74*(2), 333–351. https://doi.org/10.1175/jas-d-16-0124.1
Said, F., Jelenak, Z., Park, J., Soisuvarn, S., & Chang, P. S. (2019). A "track-wise" wind retrieval algorithm for the CYGNSS mission. *Paper presented at the IGARSS 2019-2019 IEEE International Geoscience and Remote sensing Symposium* (pp. 8711–8714). https://doi.org/10.1109/IGARSS.2019.8898099
Seager, R., Ting, M., Held, I., Kushnir, Y., Lu, J., Vecchi, G., et al. (2007). Model projections of an imminent transition to a more arid climate in southwestern North America. *Science*, *316*(5828), 1181–1184. https://doi.org/10.1126/science.1139601
Serra, Y. L., Kiladis, G. N., & Hodges, K. I. (2010). Tracking and mean structure of easterly waves over the Intra-Americas Sea. *Journal of Climate*, *23*(18), 4823–4840. https://doi.org/10.1175/2010jcli3223.1
Short, E., Vincent, C. L., & Lane, T. P. (2019). Diurnal cycle of surface winds in the maritime continent observed through satellite scatterometry. *Monthly Weather Review*, *147*(6), 2023–2044. https://doi.org/10.1175/MWR-D-18-0433.1
Sierra, J. P., Arias, P. A., Durán-Quesada, A. M., Tapias, K. A., Vieira, S. C., & Martínez, J. A. (2021). The Choco low-level jet: Past, present and future. *Climate Dynamics*, *56*(7), 2667–2692. https://doi.org/10.1007/s00382-020-05611-w
Stephens, G., Freeman, A., Richard, E., Pilewskie, P., Larkin, P., Chew, C., et al. (2020). The emerging technological revolution in Earth observations. *Bulletin of the American Meteorological Society*, *101*(3), E274–E285. https://doi.org/10.1175/bams-d-19-0146.1
Tobin, I., Bony, S., & Roca, R. (2012). Observational evidence for relationships between the degree of aggregation of deep convection, water vapor, surface fluxes, and radiation. *Journal of Climate*, *25*(20), 6885–6904. https://doi.org/10.1175/jcli-d-11-00258.1
Tompkins, A. M., & Craig, G. C. (1998). Radiative-convective equilibrium in a three-dimensional cloud-ensemble model. *Quarterly Journal of the Royal Meteorological Society*, *124*(550), 2073–2097. https://doi.org/10.1002/qj.49712455013
Torri, G., & Kuang, Z. (2016). Rain evaporation and moist patches in tropical boundary layers. *Geophysical Research Letters*, *43*, 9895–9902. https://doi.org/10.1002/2016GL070893
Trenberth, K. E., & Guillemot, C. J. (1995). Evaluation of the global atmospheric moisture budget as seen from analyses. *Journal of Climate*, *8*(9), 2255–2272. https://doi.org/10.1175/1520-0442(1995)008<2255:eotgam>2.0.co;2
Tulich, S. N., & Mapes, B. E. (2010). Transient environmental sensitivities of explicitly simulated tropical convection. *Journal of the Atmospheric Sciences*, *67*(4), 923–940. https://doi.org/10.1175/2009JAS3277.1
Ueyama, R., & Deser, C. (2008). A climatology of diurnal and semidiurnal surface wind variations over the tropical Pacific Ocean based on the tropical atmosphere ocean Moored Buoy Array. *Journal of Climate*, *21*(4), 593–607. https://doi.org/10.1175/JCLI1666.1
Vallejo-Bernal, S. M., Urrea, V., Bedoya-Soto, J. M., Posada, D., Olarte, A., Cárdenas-Posso, Y., et al. (2021). Ground validation of TRMM 3B43 V7 precipitation estimates over Colombia. Part I: Monthly and seasonal timescales. *International Journal of Climatology*, *41*(1), 601–624. https://doi.org/10.1002/joc.6640
Velasco, I., & Fritsch, J. M. (1987). Mesoscale convective complexes in the Americas. *Journal of Geophysical Research*, *92*(D8), 9591–9613. https://doi.org/10.1029/JD092iD08p09591
Vincent, C. L., & Lane, T. P. (2016). Evolution of the diurnal precipitation cycle with the passage of a Madden-Julian oscillation event through the maritime continent. *Monthly Weather Review*, *144*(5), 1983–2005. https://doi.org/10.1175/mwr-d-15-0326.1
Vincent, C. L., & Lane, T. P. (2017). A 10-year Austral summer climatology of observed and modeled intraseasonal, mesoscale, and diurnal variations over the maritime continent. *Journal of Climate*, *30*(10), 3807–3828. https://doi.org/10.1175/JCLI-D-16-0688.1
Wang, C. (2007). Variability of the Caribbean low-level jet and its relations to climate. *Climate Dynamics*, *29*(4), 411–422. https://doi.org/10.1007/s00382-007-0243-z
Wang, C., Lee, S.-K., & Enfield, D. B. (2007). Impact of the Atlantic warm pool on the summer climate of the Western Hemisphere. *Journal of Climate*, *20*(20), 5021–5040. https://doi.org/10.1175/jcli4304.1

Wang, T., Ruf, C. S., Gleason, S., O'Brien, A. J., McKague, D. S., Block, B. P., & Russel, A. (2022). Dynamic calibration of GPS effective isotropic radiated power for GNSS-Reflectometry Earth Remote Sensing. *IEEE Transactions on Geoscience and Remote Sensing*, *60*, 1–12. https://doi.org/10.1109/TGRS.2021.3070238

Warner, T. T., Mapes, B. E., & Xu, M. (2003). Diurnal patterns of rainfall in northwestern South America. Part II: Model simulations. *Monthly Weather Review*, *131*(5), 813–829. https://doi.org/10.1175/1520-0493(2003)131<0813:DPORIN>2.0.CO;2

Wei, Y., & Pu, Z. (2022). Diurnal cycle of precipitation and near-surface atmospheric conditions over the maritime continent: Land-sea contrast and impacts of ambient winds in cloud-permitting simulations. *Climate Dynamics*, *58*(9), 2421–2449. https://doi.org/10.1007/s00382-021-06012-3

Weissman, D. E., Stiles, B. W., Hristova-Veleva, S. M., Long, D. G., Smith, D. K., Hilburn, K. A., & Jones, W. L. (2012). Challenges to satellite sensors of ocean winds: Addressing precipitation effects. *Journal of Atmospheric and Oceanic Technology*, *29*(3), 356–374. https://doi.org/10.1175/jtech-d-11-00054.1

Wentz, F. J., Cardone, V. J., & Fedor, L. S. (1982). Intercomparison of wind speeds inferred by the SASS, altimeter, and SMMR. *Journal of Geophysical Research*, *87*(C5), 3378–3384. https://doi.org/10.1029/JC087iC05p03378

Whitaker, J. W., & Maloney, E. D. (2020). Genesis of an east Pacific easterly wave from a Panama Bight MCS: A case study analysis from June 2012. *Journal of the Atmospheric Sciences*, *77*(10), 3567–3584. https://doi.org/10.1175/jas-d-20-0032.1

Whyte, F. S., Taylor, M. A., Stephenson, T. S., & Campbell, J. D. (2008). Features of the Caribbean low level jet. *International Journal of Climatology*, *28*(1), 119–128. https://doi.org/10.1002/joc.1510

Wing, A. A., & Cronin, T. W. (2016). Self-aggregation of convection in long channel geometry. *Quarterly Journal of the Royal Meteorological Society*, *142*(694), 1–15. https://doi.org/10.1002/qj.2628

Wing, A. A., & Emanuel, K. A. (2014). Physical mechanisms controlling self-aggregation of convection in idealized numerical modeling simulations. *Journal of Advances in Modeling Earth Systems*, *6*, 59–74. https://doi.org/10.1002/2013MS000269

Wu, P., Manabu, D. Y., & Matsumoto, J. (2008). The formation of nocturnal rainfall offshore from convection over Western Kalimantan (Borneo) Island. *Journal of the Meteorological Society of Japan. Series II*, *86A*, 187–203. https://doi.org/10.2151/jmsj.86a.187

Wu, X., & Guimond, S. (2006). Two- and three-dimensional cloud-resolving model simulations of the mesoscale enhancement of surface heat fluxes by precipitating deep convection. *Journal of Climate*, *19*(1), 139–149. https://doi.org/10.1175/JCL3610.1

Yepes, J., Mejía, J. F., Mapes, B., & Poveda, G. (2020). Gravity waves and other mechanisms modulating the diurnal precipitation over one of the rainiest spots on Earth: Observations and simulations in 2016. *Monthly Weather Review*, *148*(9), 3933–3950. https://doi.org/10.1175/mwr-d-19-0405.1

Yepes, J., Poveda, G., Mejía, J. F., Moreno, L., & Rueda, C. (2019). CHOCO-JEX: A research experiment focused on the Chocó low-level jet over the far eastern Pacific and Western Colombia. *Bulletin of the American Meteorological Society*, *100*(5), 779–796. https://doi.org/10.1175/bams-d-18-0045.1

Yokoi, S., Katsumata, M., & Yoneyama, K. (2014). Variability in surface meteorology and air-sea fluxes due to cumulus convective systems observed during CINDY/DYNAMO. *Journal of Geophysical Research: Atmospheres*, *119*, 2064–2078. https://doi.org/10.1002/2013JD020621

Yokoi, S., Mori, S., Katsumata, M., Geng, B., Yasunaga, K., Syamsudin, F., et al. (2017). Diurnal cycle of precipitation observed in the Western coastal area of Sumatra Island: Offshore preconditioning by gravity waves. *Monthly Weather Review*, *145*(9), 3745–3761. https://doi.org/10.1175/mwr-d-16-0468.1

Young, G. S., Perugini, S. M., & Fairall, C. W. (1995). Convective wakes in the equatorial Western Pacific during TOGA. *Monthly Weather Review*, *123*(1), 110–123. https://doi.org/10.1175/1520-0493(1995)123<0110:cwitew>2.0.co;2

Zhou, L., & Wang, Y. (2006). Tropical Rainfall Measuring Mission observation and regional model study of precipitation diurnal cycle in the New Guinean region. *Journal of Geophysical Research*, *111*, D17104. https://doi.org/10.1029/2006JD007243

Zuluaga, M. D., & Houze, R. A. (2015). Extreme convection of the near-equatorial Americas, Africa, and adjoining oceans as seen by TRMM. *Monthly Weather Review*, *143*(1), 298–316. https://doi.org/10.1175/mwr-d-14-00109.1